Surface Constraints on the Depth of the Atlantic Meridional Overturning Circulation: Southern Ocean versus North Atlantic

SHANTONG SUN AND IAN EISENMAN

Scripps Institution of Oceanography, University of California, San Diego, La Jolla, California

LAURE ZANNA

Department of Physics, University of Oxford, Oxford, United Kingdom, and Courant Institute of Mathematical Sciences, New York University, New York, New York

ANDREW L. STEWART

Department of Atmospheric and Oceanic Sciences, University of California, Los Angeles, Los Angeles, California

(Manuscript received 19 July 2019, in final form 31 January 2020)

ABSTRACT

Paleoclimate proxy evidence suggests that the Atlantic meridional overturning circulation (AMOC) was about 1000 m shallower at the Last Glacial Maximum (LGM) compared to the present. Yet it remains unresolved what caused this glacial shoaling of the AMOC, and many climate models instead simulate a deeper AMOC under LGM forcing. While some studies suggest that Southern Ocean surface buoyancy forcing controls the AMOC depth, others have suggested alternatively that North Atlantic surface forcing or interior diabatic mixing plays the dominant role. To investigate the key processes that set the AMOC depth, here we carry out a number of MITgcm ocean-only simulations with surface forcing fields specified from the simulation results of three coupled climate models that span much of the range of glacial AMOC depth changes in phase 3 of the Paleoclimate Model Intercomparison Project (PMIP3). We find that the MITgcm simulations successfully reproduce the changes in AMOC depth between glacial and modern conditions simulated in these three PMIP3 models. By varying the restoring time scale in the surface forcing, we show that the AMOC depth is more strongly constrained by the surface density field than the surface buoyancy flux field. Based on these results, we propose a mechanism by which the surface density fields in the high latitudes of both hemispheres are connected to the AMOC depth. We illustrate the mechanism using MITgcm simulations with idealized surface forcing perturbations as well as an idealized conceptual geometric model. These results suggest that the AMOC depth is largely determined by the surface density fields in both the North Atlantic and the Southern Ocean.

1. Introduction

The meridional overturning circulation in the Atlantic Ocean is composed of two overturning circulation cells: an upper cell, normally referred to as the Atlantic meridional overturning circulation (AMOC), which advects the North Atlantic Deep Water (NADW) southward from the North Atlantic, and a lower cell that transports the Antarctic Bottom Water (AABW) northward from the Southern Ocean (e.g., Lumpkin and Speer 2007). In the modern climate, the upper cell extends to approximately 3000 m below the surface throughout most of the Atlantic Ocean (Lozier 2012). At the Last Glacial Maximum (LGM) about 21 000 years ago, however, studies based on paleoclimate proxy data suggest that the AMOC depth was substantially shallower (e.g., Lund et al. 2011), although this is debated (Gebbie 2014). This shoaling of the AMOC has been suggested to contribute to the lower atmospheric CO_2 at the LGM by increasing the carbon storage in the ocean (e.g., Watson et al. 2015; Ferrari et al. 2014), along with other factors (Hain et al. 2010).

Supplemental information related to this paper is available at the Journals Online website: https://doi.org/10.1175/JCLI-D-19-0546.s1.

Corresponding author: Shantong Sun, shantong@ucsd.edu

DOI: 10.1175/JCLI-D-19-0546.1

There have been concerted efforts to simulate the glacial–interglacial changes in the AMOC depth using comprehensive coupled climate models, which have led to widely varying results (e.g., Otto-Bliesner et al. 2007; Muglia and Schmittner 2015). For example, in phase 3 of the Paleoclimate Model Intercomparison Project (PMIP3), only the NCAR Community Climate System Model (CCSM4) simulated a shallower AMOC at the LGM compared with the simulated preindustrial (PI) climate, and most of the other models simulated a deeper and stronger AMOC at the LGM (Muglia and Schmittner 2015). Previous studies have attributed the deeper AMOC in most of the PMIP3 simulations of the LGM climate to a range of different processes, including a stronger Northern Hemispheric westerly wind due to the presence of the Laurentide Ice Sheet (Muglia and Schmittner 2015) and unrealistically low levels of simulated Antarctic sea ice formation (Marzocchi and Jansen 2017). The large intermodel spread of the AMOC depth in the PMIP3 LGM simulations has also been attributed to a nonlinear response of the AMOC to changes in climate model boundary conditions and forcings, including the atmospheric CO_2 level and glacial ice sheet configuration (e.g., Klockmann et al. 2018). The situation is further complicated by the possibility that these simulations are not in equilibrium with the glacial forcing, as suggested by previous studies (Zhang et al. 2013; Marzocchi and Jansen 2017).

Much progress has been made toward understanding the deep ocean circulation based on numerical simulations and theoretical arguments (e.g., Gnanadesikan 1999; Nikurashin and Vallis 2012; Marshall and Speer 2012). By assuming an adiabatic circulation in the Southern Ocean, Ferrari et al. (2014) proposed a geometric model in which the AMOC depth is dynamically linked to the extent of surface buoyancy loss near the coast of Antarctica, which approximately coincides with the region covered by sea ice in summer. This suggests that a shallower AMOC necessarily accompanies an expansion of Southern Ocean sea ice at the LGM. However, it was later shown in a climate model that diabatic processes in the Southern Ocean, which were neglected in Ferrari et al. (2014), diminish the influence of Southern Ocean surface buoyancy forcing on the AMOC depth (Sun et al. 2018).

The surface buoyancy loss rate in the Southern Ocean has also been proposed to set the AMOC depth, based on a balance between the Southern Ocean surface buoyancy loss and the interior diapycnal buoyancy gain across the boundary between the two overturning circulation cells (Jansen and Nadeau 2016). This idea neglects the contribution from diapycnal mixing in the Southern Ocean to the buoyancy budget (cf. Sun et al. 2018) and is based on a zonally integrated perspective of the global ocean overturning circulation that neglects any potential contribution from the Indo-Pacific Ocean (cf. Newsom and Thompson 2018). Hence the extent to which the surface buoyancy loss rate in the Southern Ocean could be used to predict the AMOC depth in the real ocean remains unclear.

In addition to Southern Ocean processes, North Atlantic processes have also been suggested to influence the AMOC depth (e.g., Muglia and Schmittner 2015; Wolfe and Cessi 2014; Sun and Liu 2017; Cessi 2018). For example, Muglia and Schmittner (2015) suggested that a stronger Northern Hemisphere westerly wind would lead to an increase in northward salt transport in the North Atlantic, more active NADW formation, and thus a deeper AMOC in climate model simulations. In an idealized modeling study, Wolfe and Cessi (2014) found a nonlinear dependence of the AMOC depth and strength on the range of densities shared between the North Atlantic and the Southern Ocean surfaces. This highlights the connections between the simulated surface density and the overturning circulation, although the application of this idea to the real ocean may be limited by their simplified representation of the global ocean overturning circulation.

The goal of this study is to create a conceptual framework that connects the AMOC depth to surface processes and use it to identify the key processes responsible for the wide spread among climate model simulations of the AMOC depth at the LGM compared with the PI climate. To address this, we use a global ocean-only model with surface forcing based on PMIP3 coupled climate model simulations, as described in section 2. We find that by modifying the surface restoring time scale, we can control whether we match the PMIP3 surface buoyancy flux or surface density in our simulations, and we investigate the effects of this on the AMOC depth in section 3. The results suggest that the AMOC depth is directly connected to the surface density field in both the North Atlantic and the Southern Ocean. In section 4, we demonstrate this connection using a set of simulations with idealized perturbations to the surface density field, as well as a conceptual geometric model that relates the AMOC depth to the surface density in both regions. Further discussion and comparisons with previous theories for the AMOC depth are provided in section 5. The findings are summarized in section 6.

2. Reproducing AMOC changes in the PMIP3 simulations

In this section, we describe the ocean-only simulations and evaluate how well they reproduce the AMOC depth in the PMIP3 simulations.

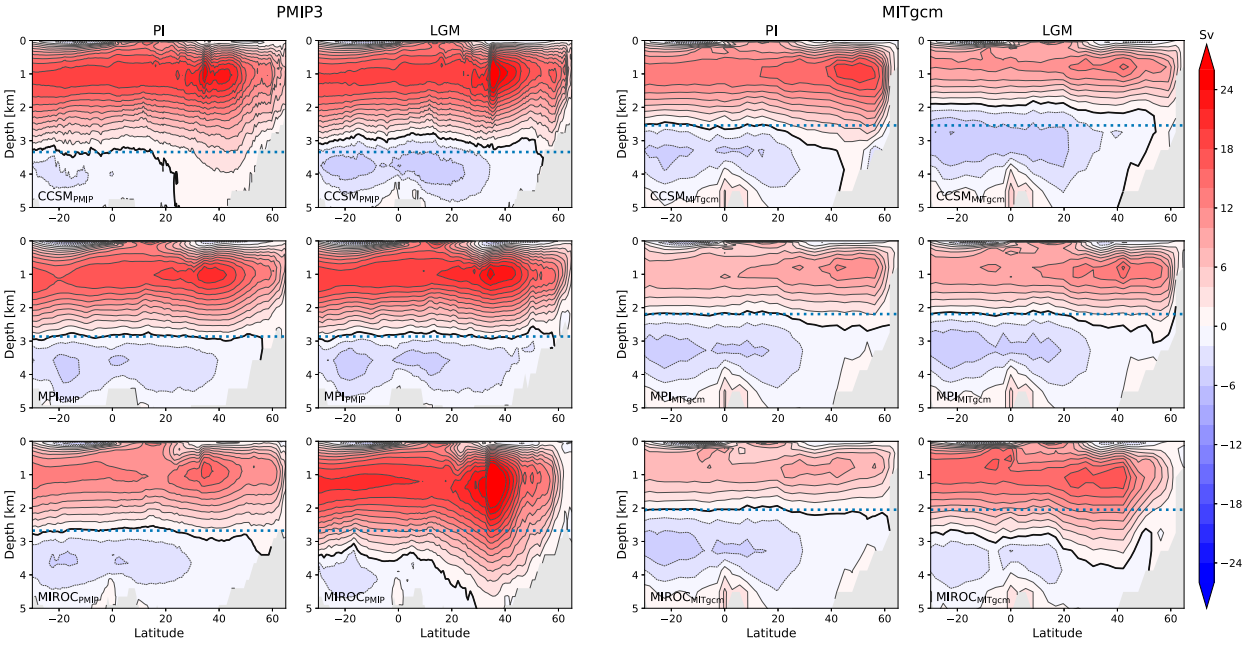

FIG. 1. Long-term mean Eulerian-mean overturning circulation streamfunction in the Atlantic Ocean $\overline{\psi}$ simulated by (left) the PMIP3 coupled models and (right) the MITgcm ocean-only model forced with the surface fields from the PMIP3 runs. The thick black contour in each panel indicates the zero streamline that separates the upper and lower overturning circulation cells in the Atlantic Ocean. The AMOC depth in each of the PI runs, as defined in Eq. (2), is indicated as a blue dotted line, which is repeated in each of the corresponding LGM runs for comparison.

a. Overturning circulation in PMIP3 simulations

PMIP3 is an effort to simulate the climate at several past time periods, including the LGM, in a number of different comprehensive climate models (Braconnot et al. 2012). For the LGM simulations, the models use prescribed glacial forcing conditions including atmospheric CO_2 levels, specified ice sheets, and orbital parameters. Details can be found in Braconnot et al. (2012).

Because most of the PMIP3 models, including two that we focus on in this study (MPI-ESM and MIROC-ESM), do not report the eddy bolus velocity in the simulation output, we use the Eulerian-mean overturning circulation streamfunction in this analysis to represent the AMOC in all of the PMIP3 models. We define the climatological Eulerian-mean overturning circulation streamfunction in the Atlantic Ocean $\overline{\psi}$ as

$$\overline{\psi}(y,z) = -\int_{z_{\rm bot}}^{z}\int_{x_w}^{x_e}\overline{v}(x,y,z')\,dx\,dz', \qquad (1)$$

where the bar indicates the Eulerian mean, x is longitudinal displacement, y is latitudinal displacement, z is depth with $z_{\rm bot}$ the depth of the ocean bottom, v is meridional velocity averaged over the final 100 years of each PMIP3 simulation, and x_w and x_e are the western and eastern boundaries of the Atlantic basin, respectively.

We define the AMOC depth as the depth of the zero contour of $\overline{\psi}$ in the Atlantic (thick black lines in Fig. 1) averaged between 30°S and the equator, as in Sun et al. (2018), that is,

$$H_{\rm Eulerian} = -\frac{1}{L_y}\int_{-L_y}^{0} z_{\rm Eulerian}(y)\,dy, \qquad (2)$$

where L_y represents the meridional distance between 30°S and the equator, and $z_{\rm Eulerian}$ is the depth of the streamline $\overline{\psi}=0$ at meridional location y such that

$$\overline{\psi}[y, z_{\rm Eulerian}(y)] = 0. \qquad (3)$$

We limit the definition to the South Atlantic because the lower overturning circulation cell is weak in the Northern Hemisphere, and the cell boundary is not well defined in some PMIP3 simulations (see, e.g., the MIROC-ESM LGM simulation in Fig. 1). The AMOC depth defined in Eq. (2) approximately represents the water mass boundary between NADW and AABW in the Atlantic Ocean. We have also used other definitions, such as the depth where the AMOC streamfunction is half of its maximum value (e.g., Muglia and Schmittner 2015), and the results are approximately insensitive to this change in definition.

In this study we focus on three of the PMIP3 models: CCSM4, MPI-ESM, and MIROC-ESM. All three of the models have a nominal ocean resolution of 1°. These models were selected because they broadly cover each of the three possibilities for AMOC depth differences between the LGM and PI climates (Fig. 1): CCSM4 simulates a shallower AMOC depth at the LGM, MPI-ESM simulates a similar AMOC depth at the LGM as the PI climate, and MIROC-ESM simulates a deeper AMOC depth at the LGM. Additionally, these three models are the only ones that reported enough simulation output data for us to create the surface forcing fields needed for the ocean-only simulations that are described in the next subsection.

b. Model setup

Investigations into the processes that set the AMOC depth in different climate models can be complicated by differences in the representations of the model physics and what output each model reports. To explore the physical constraints on the AMOC depth, here we use a single ocean-only model with surface forcing based on the PMIP3 coupled climate model simulations. This approach follows Huber and Zanna (2017), who used a similar methodology to evaluate the impact of uncertainties in air–sea fluxes and ocean model parameters on the ocean circulation and ocean heat uptake in climate model simulations of preindustrial and future climates. They found that using a single ocean-only model with surface forcing fields from the coupled climate models could adequately reproduce the mean AMOC in these models.

We use the Massachusetts Institute of Technology General Circulation Model (MITgcm; Marshall et al. 1997), which integrates the hydrostatic primitive equations. The model is configured to run at a relatively coarse resolution (2.8° × 2.8°), which allows for a relatively large number of simulations without incurring excessive computational costs. The model has an approximately realistic modern bathymetry that is equivalent to what was used by Huber and Zanna (2017). We use this bathymetry for both PI and LGM simulations, neglecting effects of the lower sea level at the LGM. There are 15 layers in the vertical with thickness ranging from 50 m at the top to 690 m at the bottom. We use a vertical diffusivity that is a function of depth and varies from $3 \times 10^{-5}\,\mathrm{m^2\,s^{-1}}$ at the surface to $1.3 \times 10^{-4}\,\mathrm{m^2\,s^{-1}}$ at the transition depth of 2000 m (Bryan and Lewis 1979). Momentum is dissipated via Laplacian horizontal viscosity and vertical viscosity with coefficients $A_h = 2.0 \times 10^5\,\mathrm{m^2\,s^{-1}}$ and $A_z = 1.0 \times 10^{-3}\,\mathrm{m^2\,s^{-1}}$, respectively. Unresolved eddies are represented using the skew-flux form of the Gent–McWilliams (GM) parameterization with an eddy thickness diffusivity of $1000\,\mathrm{m^2\,s^{-1}}$ (Griffies 1998). Convection is represented by an implicit vertical diffusion with diffusivity of $100\,\mathrm{m^2\,s^{-1}}$ whenever the stratification is unstable. We use a nonlinear equation of state for the ocean (Jackett and McDougall 1995). All simulations performed in this study are integrated for at least 6000 years in order to approximately achieve steady states, using the tracer acceleration method (Bryan 1984). Note that the tracer acceleration method can distort the transient response, but it is not expected to substantially affect the equilibrium solution (Danabasoglu et al. 1996).

The model is forced with the mean climatological seasonal cycle during the last 100 years from each of the PMIP3 simulations. Specifically, we use the PMIP3 monthly mean sea surface stress vector for the momentum forcing in the MITgcm simulations, and the buoyancy boundary conditions at the sea surface are given by

$$F_\theta = -\frac{\rho_0 c_p h_s}{\tau_\theta}(\theta - \theta^*) + Q^*_{\mathrm{net}}, \tag{4a}$$

$$F_{\mathrm{salt}} = -\frac{h_s}{\tau_{\mathrm{salt}}}(S - S^*) + F^*_{\mathrm{salt}}. \tag{4b}$$

Here, the asterisk (*) indicates climatological monthly mean fields from the PMIP3 simulations, θ is sea surface temperature, S is sea surface salinity, τ_θ and τ_{salt} are the restoring time scales for temperature and salinity, respectively, F_θ is the surface net heat flux with positive values indicating fluxes that warm the ocean, and F_{salt} represents the surface salt flux. The surface salt flux in the PMIP3 simulations is diagnosed as the net freshwater flux from precipitation, evaporation, and sea ice melting and freezing scaled by a reference salinity of $35\,\mathrm{g\,kg^{-1}}$. The thickness of the top layer is $h_s = 50\,\mathrm{m}$, and the reference seawater density and specific heat capacity are $\rho_0 = 1035\,\mathrm{kg\,m^{-3}}$ and $c_p = 3994\,\mathrm{J\,°C^{-1}\,kg^{-1}}$.

Unless otherwise specified, we use relaxation time scales for surface temperature and salinity of $\tau_\theta =$ 2 months and $\tau_{\mathrm{salt}} = 3$ months, respectively. This value of τ_θ is based on the upper-ocean relaxation time scale, following Haney (1971). For salinity, the insensitivity of the atmosphere to sea surface salinity suggests an arbitrarily long time scale, with only the specified flux term dictating the forcing. However, differences between each PMIP3 model and MITgcm are expected to give rise to different ocean advection and mixing of salt, leading to steadily growing biases in the MITgcm surface salinity field, and the salinity relaxation term serves to reduce this bias. Based on this, a value of τ_{salt} is chosen that is slightly larger than τ_θ. The values that we

adopt for τ_θ and τ_{salt} are equivalent to those used by Huber and Zanna (2017).

Therefore, the relaxation terms in Eq. (4) essentially provide a correction to the surface buoyancy flux in order to account for the simulated surface density biases due to the differences in the representation of ocean physics between MITgcm and each of the PMIP3 models. In the simplified scenario in which MITgcm has exactly the same ocean dynamics as a PMIP3 model, this correction is zero, and both the surface density and the surface buoyancy flux in the PMIP3 simulations can be reproduced in the MITgcm runs. However, due to the model differences, there is a trade-off between reproduction of the PMIP3 surface density and reproduction of the PMIP3 surface buoyancy flux in the MITgcm simulations that depends on the surface relaxation time scales (see appendix A for details). In the limit of strong relaxation (small τ_θ and τ_{salt}), the simulated surface density field in MITgcm closely follows the PMIP3 models, but the surface buoyancy flux can differ substantially due to the correction; in the limit of weak relaxation (large τ_θ and τ_{salt}), on the other hand, the correction is small and the surface buoyancy flux in MITgcm closely follows the PMIP3 models, but the simulated surface density can differ substantially. Therefore, by varying the restoring time scales (τ_θ and τ_{salt}), this form of buoyancy boundary conditions allows us to explore the relative importance of the simulated surface density versus the surface buoyancy flux in constraining the AMOC depth, as described in the next section.

We performed MITgcm simulations with surface forcing fields specified from each of the six PMIP3 simulations in Fig. 1. The Eulerian-mean AMOC streamfunction is plotted in Fig. 1 for the PMIP3 simulations (left) and for the MITgcm simulations (right). The results in Fig. 1 indicate that the MITgcm simulations qualitatively capture the AMOC depth changes between the PI and LGM climates in the PMIP3 simulations. However, each of the MITgcm simulations can be seen to underestimate the AMOC depth and strength in the corresponding PMIP3 simulation, which is similar to the results of Huber and Zanna (2017, their Fig. 2b). This underestimate may be due to differences in the physical representations and parameters in the MITgcm simulations compared with each PMIP3 model, as was discussed for preindustrial and future simulated climates by Huber and Zanna (2017, their Fig. 4). For example, we use a GM thickness diffusivity of 1000 $m^2 s^{-1}$ in order to suppress grid noise at the relatively coarse resolution in MITgcm, and this is about 3 times larger than the default background value in each of the three PMIP3 models (Danabasoglu et al. 2012; Watanabe et al. 2010; Exarchou et al. 2015). This larger GM thickness diffusivity can weaken and shoal the AMOC due to its effect on the compensation of the wind-driven overturning circulation in the Southern Ocean (Marshall et al. 2017). Additionally, the Nordic seas overflows, which have been suggested to deepen the AMOC depth in model simulations (Danabasoglu et al. 2010; Nakano and Suginohara 2002; Marsland et al. 2003), are not represented in MITgcm but are parameterized in each of the three PMIP3 models. This could also contribute to the underestimated depth and strength of the AMOC in the MITgcm simulations. In the following analysis, we will focus on changes in the AMOC depth between the PI and LGM climates, which are better reproduced in the MITgcm simulations than the AMOC depth in each climate.

3. Reproducing the PMIP3 AMOC depth changes in MITgcm: Surface density versus surface buoyancy flux

In this section, we use the ocean-only MITgcm configuration described in section 2b to investigate the possibility that the global surface density distribution is the dominant factor in determining the intermodel spread of the glacial AMOC depth changes among the PMIP3 models (cf. Nikurashin and Vallis 2012; Wolfe and Cessi 2014; Sun and Liu 2017). Figure 2 shows the difference in surface density between the simulated LGM and PI climates in the three PMIP3 models. The surface density difference field tends to be more positive in the subpolar North Atlantic (40°–60°N) than in the Southern Ocean (south of 50°S). This difference between the North Atlantic and Southern Oceans is greatest in MIROC-ESM, which simulates a deepening of the AMOC at the LGM, and it is smallest in CCSM4, which has a shoaling of the AMOC at the LGM. Indeed, the other PMIP3 models that simulate a deeper AMOC at the LGM also tend to have surface density changes from PI to LGM in the Atlantic compared to the Southern Ocean that resemble MIROC-ESM (not shown). This suggests the possible importance of this feature of the simulated surface density field for explaining the intermodel differences in AMOC depth among the PMIP3 models. The surface buoyancy flux fields are shown for comparison in Fig. S1 in the online supplemental material.

We evaluate the importance of the surface density distribution compared with the surface buoyancy flux distribution for constraining the AMOC depth by varying the restoring time scales in Eq. (4). In addition to the six MITgcm simulations described in section 2b above (“medium”: τ_θ = 2 months and τ_{salt} = 3 months), we carried out an additional set of six simulations with

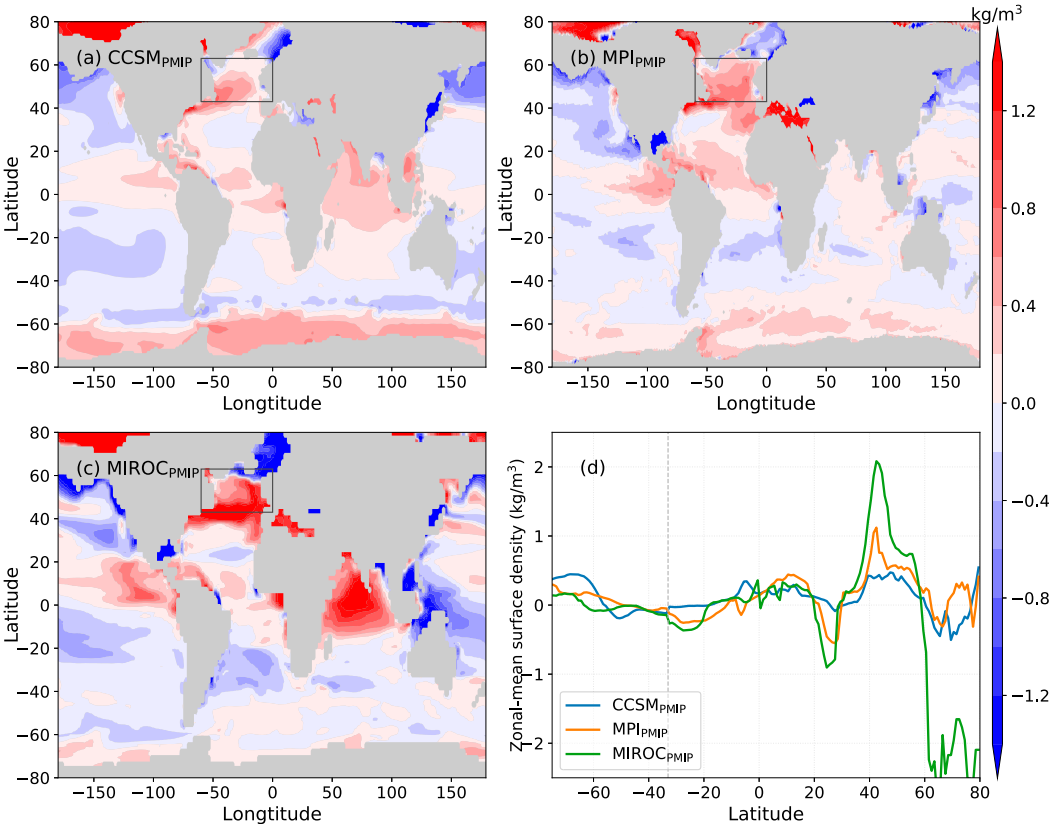

FIG. 2. (a)–(c) Difference in the annual-mean surface density between the PMIP3 simulated LGM and PI climates (LGM minus PI) in CCSM4, MPI-ESM, and MIROC-ESM. In each panel, the global average has been subtracted to highlight the regional distributions. The rectangle in each panel indicates the subpolar North Atlantic, where most of the NADW formation occurs in the PMIP3 models. (d) Annual-mean zonal-mean values of the surface density differences. The zonal averages are calculated over the full range of longitudes south of 33°S but only in the Atlantic Ocean north of 33°S, with a gray dashed line indicating 33°S. As in the other panels, the global-mean values have been subtracted from each curve.

stronger relaxation ("strong": τ_θ = 12 days and τ_{salt} = 18 days) and six simulations with weaker relaxation ("weak": τ_θ = 10 months and τ_{salt} = 15 months). As shown in Fig. 3, with strong relaxation (small τ_θ and τ_{salt}) the surface density simulated in MITgcm approximately reproduces the prescribed surface density, but the surface buoyancy flux simulated in MITgcm tends to differ substantially from the PMIP3 simulations. With weak relaxation (large τ_θ and τ_{salt}), on the other hand, the surface buoyancy fluxes approximately match but the surface densities tend to differ substantially. The reason for this behavior can be readily surmised from Eq. (4): in the former case the relaxation terms dominate, which leads to the temperature and salinity in MITgcm matching PMIP3, and in the latter case the relaxation terms are negligible and the fluxes in MITgcm match PMIP3. The influence of varying the restoring time scales is discussed in more detail in appendix A.

The MITgcm runs with strong and medium relaxation largely reproduce the LGM–PI AMOC depth changes in the PMIP3 simulations (Fig. 4b), although the MITgcm simulations underestimate the AMOC depth in all of the individual PMIP3 simulations (Fig. 4a). The MITgcm runs with weak relaxation underestimate the AMOC deepening at the LGM by 700 m for MIROC-ESM, simulate a shoaling of 300 m at the LGM for MPI-ESM, which has approximately no change in PMIP3, and overestimate the shoaling at the LGM by 240 m for CCSM. The MITgcm runs with medium relaxation closely reproduce the AMOC depth changes for both MPI-ESM and MIROC-ESM within 50 m, but they overestimate the shoaling for CCSM by 230 m at the LGM. The MITgcm runs with strong relaxation reproduce the AMOC depth changes for CCSM and MPI-ESM within 50 m, but they overestimate the AMOC deepening by 350 m for MIROC-ESM.

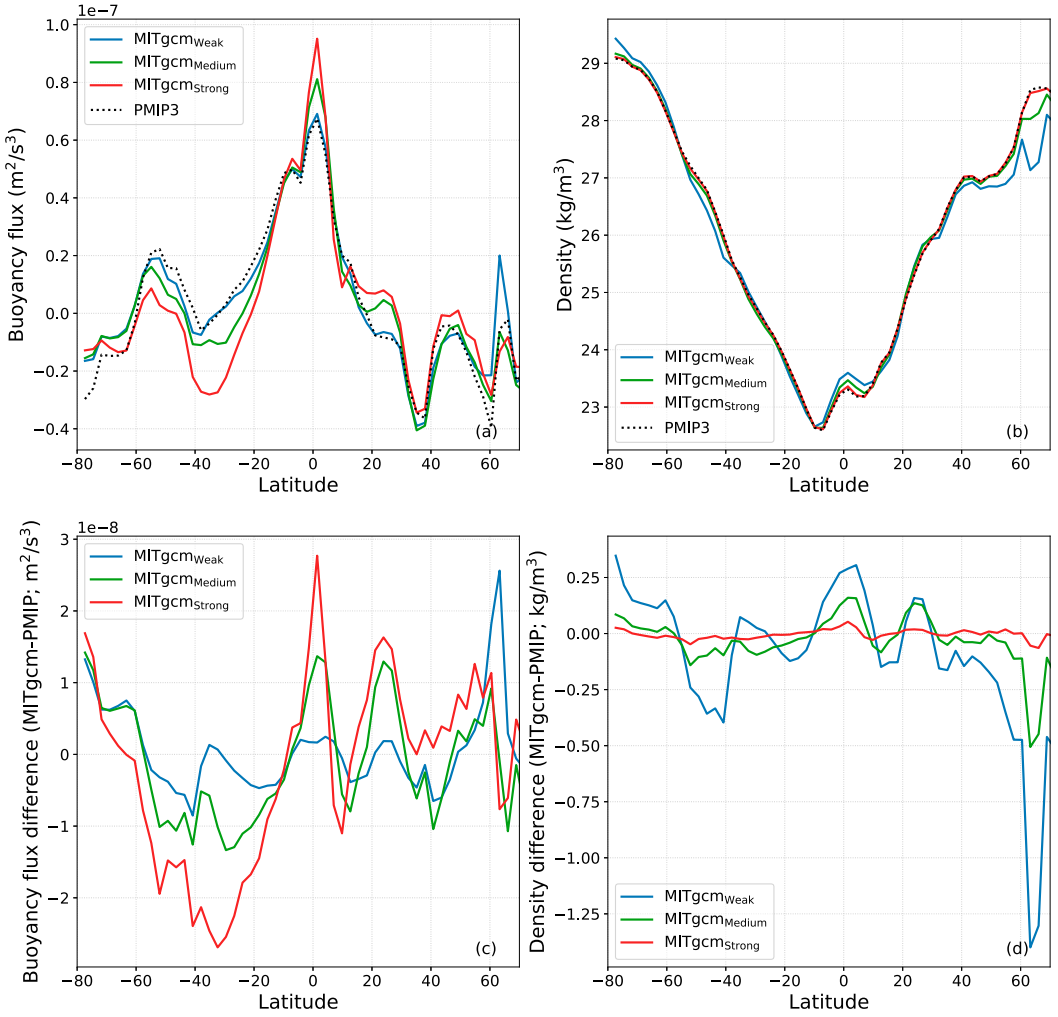

FIG. 3. Zonal-mean (a) surface buoyancy flux and (b) surface density in the CCSM4 PMIP3 simulation of the LGM climate (dotted lines) and in the MITgcm runs with surface forcing from the CCSM4 PMIP3 simulation and varied restoring strengths (solid lines). (c),(d) The differences between each MITgcm run and the CCSM4 PMIP3 simulation. The MITgcm runs with stronger relaxation tend to more closely reproduce the surface density and less closely reproduce the surface buoyancy flux, as described in the text. Here the surface buoyancy flux is calculated as $F = (g/\rho_0)(\alpha F_\theta/c_p - \rho_0 \beta F_{\text{salt}})$, where g is gravitational acceleration, α is the thermal expansion coefficient, and β is the haline contraction coefficient.

Hence the results in Fig. 4b show that the simulations with weak relaxation, which most closely reproduce the surface buoyancy flux in the PMIP3 simulations, do a substantially worse job of reproducing the LGM–PI changes in the AMOC depth than the simulations with stronger relaxation, which most closely reproduce the surface density distribution in the PMIP3 simulations. This suggests that the simulated LGM–PI changes in AMOC depth in the PMIP3 simulations are closely connected to the simulated surface density field. This stands in contrast with previous emphasis on surface buoyancy flux in controlling the AMOC depth (e.g., Ferrari et al. 2014; Jansen and Nadeau 2016), which is further discussed in section 5.

The three PMIP3 models discussed in this paper followed different procedures for their initialization and spinup processes for the coupled LGM simulations (Brady et al. 2013; Mikolajewicz et al. 2012; Sueyoshi et al. 2013). Thus these coupled simulations may be subject to different levels of equilibration, and this may help account for the different levels of improvement in the simulated LGM–PI AMOC depth changes when we increase the relaxation strength in MITgcm. Marzocchi and Jansen (2017) found that the AMOC depth in the CCSM4 LGM simulation shoals by an additional 100 m

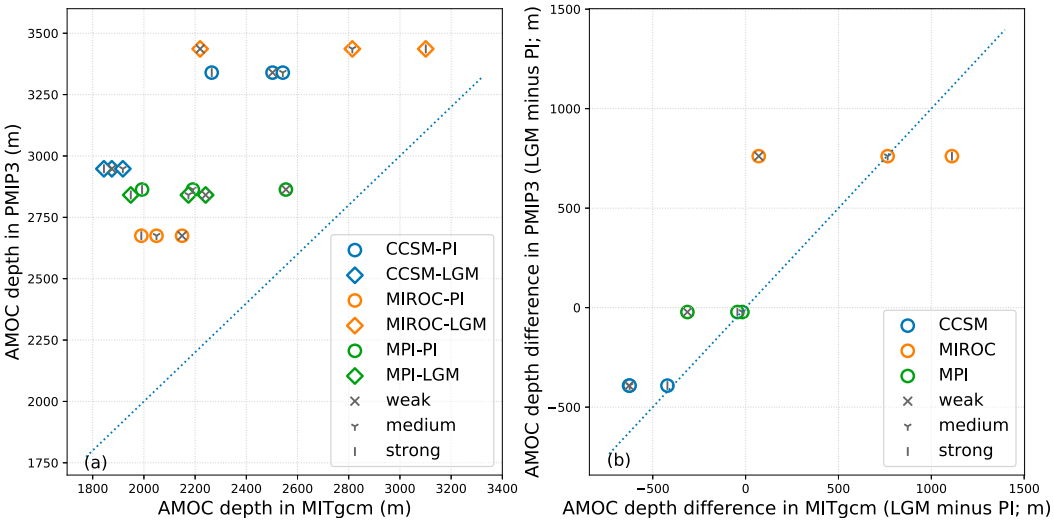

FIG. 4. Comparison between the PMIP3 simulations and the three sets of MITgcm simulations with varied relaxation strengths in terms of (a) the LGM and PI AMOC depth and (b) the LGM–PI AMOC depth difference. The results are plotted with the PMIP3 output on the vertical axis and the MITgcm simulation results on the horizontal axis. The shapes of the gray symbols indicate the level of relaxation, the shapes of colored symbols enclosing the gray symbols indicate LGM or PI, and the colors of these symbols indicate the PMIP3 model that was used for the surface forcing. The blue dotted line in each panel represents equality between the quantities on the vertical and horizontal axes. Note that in (b) the weak and medium CCSM cases are overlapping.

during the 500 simulation years following the period reported in PMIP3. However, this amount of shoaling is much smaller than the approximate 1200-m intermodel spread in the simulated LGM–PI AMOC depth changes among the PMIP3 simulations considered here.

As discussed in previous studies (e.g., Gnanadesikan 1999; Marshall and Zanna 2014; Nikurashin and Vallis 2012; Marshall et al. 2017), the strength of the AMOC is strongly correlated with its depth (Fig. S2). This suggests that the AMOC strength is also strongly connected to the surface density field. Consistent with this, the surface density field has been used to construct scaling laws for the AMOC strength in previous studies (e.g., Gnanadesikan 1999; Wolfe and Cessi 2011; Nikurashin and Vallis 2012).

4. Surface density constraints on AMOC depth

In this section, we investigate how the surface density field constrains the AMOC depth. We carry out a series of idealized perturbation simulations with MITgcm and then construct a geometric model that relates the AMOC depth to the surface density field in the North Atlantic as well as the Southern Ocean.

a. Idealized perturbation runs

We carry out a series of simulations with perturbed surface density fields in the North Atlantic and the Southern Ocean, since these are the two regions where the deep ocean primarily ventilates. The MITgcm simulation with the surface forcing derived from the CCSM4 PMIP3 PI run is adopted as the reference simulation, except that in this series of simulations we use a very strong relaxation (τ_θ = 6 days and $\tau_{\rm salt}$ = 9 days) such that the simulated surface density closely follows the restoring surface density. We perturb the surface density by adding a salinity perturbation to the restoring surface salinity field, replacing Eq. (4b) with

$$F_{\rm salt} = -\frac{h_s}{\tau_{\rm salt}}[S - (S^* + \Delta S^*_N P_N + \Delta S^*_S P_S)] + F^*_{\rm salt}, \quad (5)$$

where ΔS^*_N and ΔS^*_S are scalar parameters with units of salinity that control the magnitude of the salinity perturbations, and P_N and P_S are dimensionless fields that represent the geographical distribution of the salinity perturbations. As indicated in Fig. 5, the North Atlantic perturbation field P_N is 1 to the north of 40°N in the Atlantic Ocean and decreases linearly southward to a value of 0 at 20°N, and the Southern Ocean perturbation field P_S is 1 to the south of 40°S and decreases linearly northward to a value of 0 at 20°S. We use salinity instead of temperature to perturb the surface density because the haline contraction coefficient β is relatively constant with respect to varying temperature and salinity. For example, if the temperature varies spatially from −2° to

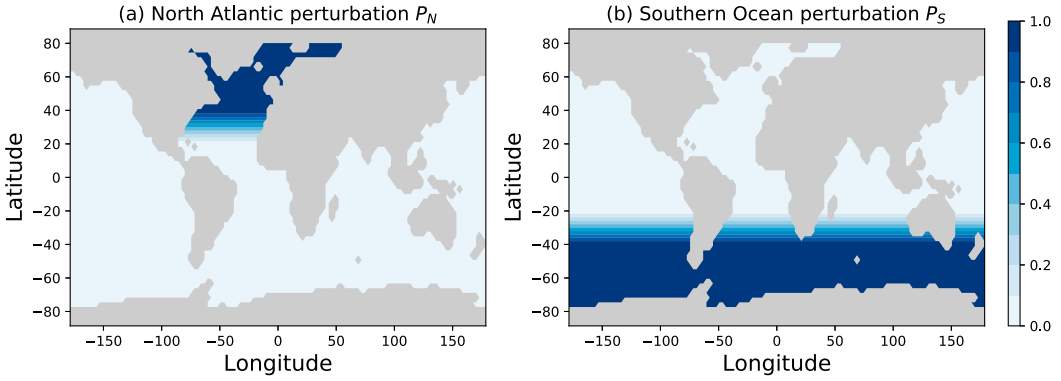

FIG. 5. Salinity perturbation distributions in (a) the North Atlantic P_N and (b) the Southern Ocean P_S.

10°C and the salinity remains at 35 g kg^{-1} at the sea surface, β varies from 7.93×10^{-4} to 7.65×10^{-4} (g kg^{-1})$^{-1}$, whereas the thermal expansion coefficient α varies from 0.4×10^{-4} to 1.67×10^{-4} °C^{-1}. Consequently, a salinity perturbation represents roughly the same surface density perturbation in the North Atlantic as in the Southern Ocean. In the following discussions, we will assume $\beta = 7.8 \times 10^{-4}$ (g kg^{-1})$^{-1}$ to translate the salinity perturbations to density perturbations.

Four sets of idealized perturbation runs are performed (Table 1): North Atlantic, Southern Ocean, Symmetric, and Antisymmetric. The perturbations are uniform in the high latitudes (Fig. 5), which ensures that the deep convection occurs at approximately unchanged locations in the North Atlantic and the Southern Ocean as the salinity perturbations are varied. As a result, changes in the density of NADW and AABW in their source locations follow the surface perturbations in the North Atlantic and the Southern Ocean regions, respectively. For example, in the North Atlantic perturbation runs, we show in Fig. 6b that the AABW density stays approximately constant and changes in the NADW density are approximately equal to the values of the surface perturbations in the North Atlantic.

In the analysis of the PMIP3 simulations above, we used the Eulerian-mean overturning circulation streamfunction $\overline{\psi}$ to represent the overturning circulation because most of the PMIP3 models did not report the eddy bolus velocity. Here, because MITgcm does report this, we instead analyze the isopycnal overturning circulation streamfunction ψ, which includes contributions from both the mean flow and the parameterized eddies. The isopycnal overturning circulation streamfunction ψ provides a more accurate representation of the overturning circulation (e.g., Karsten and Marshall 2002). It is not substantially different from the Eulerian mean in the Atlantic basin (except in regions of deep convection) due to the relatively small role played there by eddies, but it differs more substantially in the Southern Ocean where eddies play a larger role (e.g., Marshall and Radko 2003). We present our definition of the AMOC depth based on the isopycnal overturning circulation in appendix B. The AMOC depth H_{isop} defined based on the isopycnal overturning circulation is approximately the same as that defined using the Eulerian-mean overturning circulation [H_{Eulerian} in Eq. (2); see Fig. S3].

We present the AMOC depth in the four sets of idealized perturbation runs in Fig. 7a, where the AMOC depth is plotted against the difference between the perturbation to the North Atlantic surface salinity and the perturbation to the Southern Ocean surface salinity. The four sets of perturbation runs approximately fall on a single curve, suggesting that changes in the AMOC depth can be expressed as a function of the surface

TABLE 1. Summary of the four sets of idealized perturbation runs discussed in section 4. The first column indicates the name of the set, the second column indicates the range of values scaling the perturbation to the North Atlantic salinity, and the third column indicates the range of values scaling the perturbation to the Southern Ocean salinity. These represent the full ranges over which the AMOC reaches the Southern Ocean but does not reach the ocean bottom: for $\Delta S_N^* > 0.3$ g kg^{-1} in the North Atlantic perturbation runs, $\Delta S_S^* < -0.3$ g kg^{-1} in the Southern Ocean perturbation runs, and $\Delta S_N^* > 0.15$ g kg^{-1} in the Antisymmetric perturbation runs, the AMOC reaches the ocean bottom; and for $\Delta S_N^* < -0.6$ g kg^{-1} in the North Atlantic perturbation runs, $\Delta S_S^* > 0.6$ g kg^{-1} in the Southern Ocean perturbation runs, and $\Delta S_N^* < -0.3$ g kg^{-1} in the Antisymmetric perturbation runs, the AMOC does not reach the Southern Ocean.

Perturbation runs	ΔS_N^* (g kg^{-1})	ΔS_S^* (g kg^{-1})
North Atlantic	−0.6 to 0.3	0
Southern Ocean	0	−0.3 to 0.6
Symmetric	−0.6 to 0.3	$\Delta S_S^* = \Delta S_N^*$
Antisymmetric	−0.3 to 0.1	$\Delta S_S^* = -\Delta S_N^*$

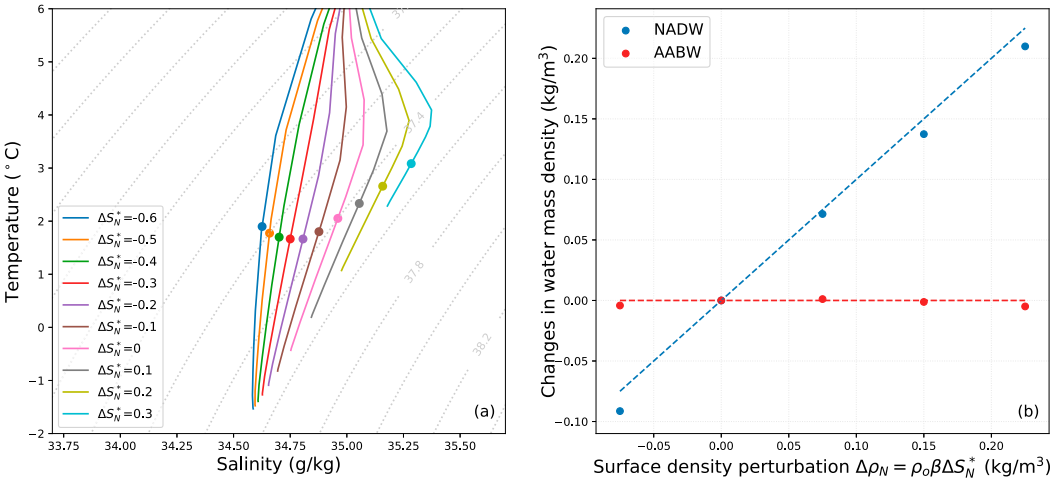

FIG. 6. (a) Temperature–salinity diagram for the North Atlantic perturbation runs. This diagram is obtained by averaging the time-averaged temperature and salinity fields on constant depth levels between 20°S and 20°N in the Atlantic Ocean. Water masses with temperature higher than 6°C are not shown. The dots represent the isopycnal that separates the two overturning circulation cells in the Atlantic Ocean [defined in Eq. (6)]. Contours of σ_2 are indicated as gray dotted lines. (b) Change in potential density of the NADW core and AABW in the North Atlantic perturbation runs with $\Delta S_N^* \geq -0.1$ g kg^{-1}. The NADW core is characterized by a salinity maximum in the temperature–salinity diagram for the deep ocean, and it is defined here as the maximum salinity in the diagram plotted in (a). The density of AABW is defined as the maximum of the potential density profile averaged between 20°S and 20°N in the Atlantic Ocean. Note that for the runs with $\Delta S_N^* < -0.1$ g kg^{-1}, which are not included here, the NADW core is too fresh and too shallow, and there is no interior salinity maximum in the temperature-salinity diagram. The blue dashed line in (b) represents equality between the vertical and horizontal plotted quantities, and the red dashed line represents zero water mass density change.

density perturbation difference between the North Atlantic and the Southern Ocean alone. In the following subsection, we construct a geometric model to explore this relationship.

b. *Geometric model*

We define the potential density of the isopycnal contour that separates the two overturning circulation cells in the Atlantic Ocean (ρ_{bdry}) implicitly as

$$\int_{-L_y}^{0} \psi_{\text{atl}}(y, \rho_{\text{bdry}})\, dy = 0. \tag{6}$$

This isopycnal ρ_{bdry} approximately represents the water mass boundary between NADW and AABW (dots in Fig. 6a), and the zero overturning circulation streamlines closely follows this isopycnal contour across the Atlantic Ocean (Fig. 8). In the geometric model that we develop here, we use the depth of this isopycnal boundary in the Atlantic Ocean to represent the AMOC depth and denote it as H, which is a close approximation to H_{isop} (Fig. 8) and hence also to H_{Eulerian}.

The depth H of the isopycnal ρ_{bdry} that separates the two overturning circulation cells at the northern boundary of the Southern Ocean can be related to the horizontal distribution of surface density in the Southern Ocean. The AMOC depth can be characterized in terms of the latitudinal location y_b where the isopcyanl boundary outcrops in the Southern Ocean as

$$H = s(y_b - y_0), \tag{7}$$

where s is the slope of isopycnals in the Southern Ocean, which we approximate here as constant, and y_0 is the latitudinal location of the northern boundary of Southern Ocean (approximately 30°S). For the control run ($\Delta S_N^* = \Delta S_S^* = 0$), the isopycnal boundary ρ_{bdry}^c outcrops at y_b^c in the Southern Ocean, where the superscript denotes the model run, and we have

$$R_h(y_b^c) = \rho_{\text{bdry}}^c, \tag{8}$$

where R_h is the horizontal zonal-mean surface density profile in the Southern Ocean in the control run.

In each idealized perturbation run, the horizontal profile of surface density in the Southern Ocean has a spatially constant difference from the control run of $\Delta\rho_S = \rho_0 \beta \Delta S_S^*$, and hence the isopycnal boundary ρ_{bdry}^p outcrops at the location y_b^p that satisfies

$$R_h(y_b^p) + \Delta\rho_S = \rho_{\text{bdry}}^p. \tag{9}$$

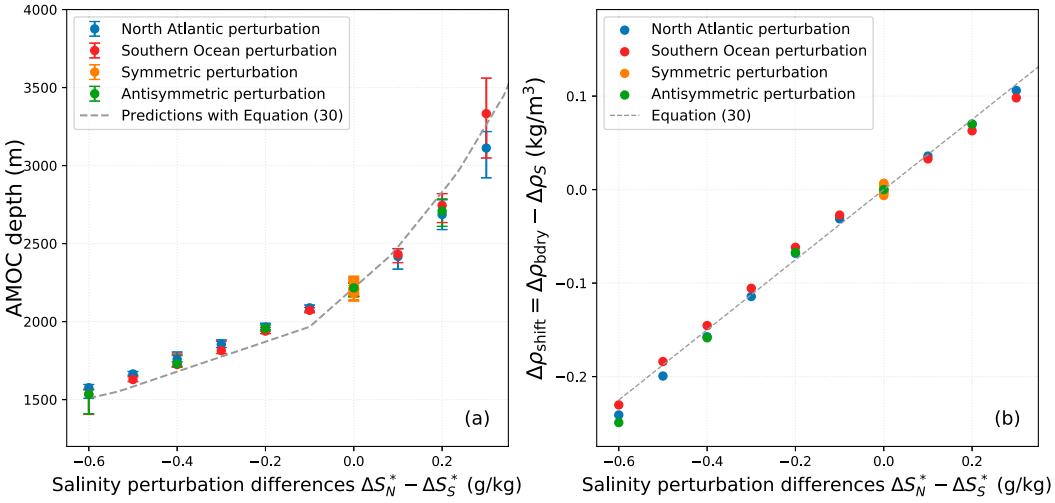

FIG. 7. The isopycnal overturning circulation streamfunction ψ mapped to depth coordinates in the Atlantic Ocean in each of the North Atlantic perturbation runs. The value of the salinity perturbation parameter (g kg^{-1}) is indicated in each panel. The thick black line in each panel represents the isopycnal contour ρ_{bdry} that separates the two overturning circulation cells in the Atlantic Ocean. Note that the overturning circulation streamfunction in each of the Southern Ocean perturbation runs (not shown) is approximately equivalent to the North Atlantic perturbation run with the opposite perturbation parameter value, e.g., the Southern Ocean perturbation run with $\Delta S_S^* = 0.6$ g kg^{-1} has an overturning circulation streamfunction approximately equivalent to the North Atlantic perturbation run with $\Delta S_N^* = -0.6$ g kg^{-1}.

Subtracting Eq. (8) from Eq. (9) gives

$$R_h(y_b^p) - R_h(y_b^c) = \Delta\rho_{\text{shift}}, \tag{10}$$

where we define

$$\Delta\rho_{\text{shift}} \equiv \Delta\rho_{\text{bdry}} - \Delta\rho_S, \tag{11}$$

and

$$\Delta\rho_{\text{bdry}} \equiv \rho^p_{\text{bdry}} - \rho^c_{\text{bdry}}. \tag{12}$$

Here $\Delta\rho_{\text{bdry}}$ represents the change in the potential density of the isopycnal boundary between the perturbation run and the control run, and $\Delta\rho_{\text{shift}}$ represents the change in the density of the isopycnal boundary $\Delta\rho_{\text{bdry}}$ relative to the density perturbation in the Southern Ocean $\Delta\rho_S$. The variable $\Delta\rho_{\text{shift}}$ is related to how the outcrop position in the Southern Ocean of the isopycnal ρ_{bdry} shifts in a given perturbation run [Eq. (10)].

Assuming that the isopycnal slope remains approximately constant under perturbations to the Southern Ocean surface density (e.g., Böning et al. 2008; Gent and Danabasoglu 2011) and combining Eqs. (7) and (10), the difference in the AMOC depth between a given perturbation run and the control run can be approximated as

$$\begin{aligned}\Delta H &\approx s(y_b^p - y_b^c)\\ &\approx \frac{s\Delta\rho_{\text{shift}}}{(dR_h/dy)|_{y_b^c}},\end{aligned} \tag{13}$$

where the first approximation assumes constant isopycnal slope and the second uses a first-order Taylor expansion of R_h around y^c,

$$R_h(y_b^p) - R_h(y_b^c) \approx \left.\frac{dR_h}{dy}\right|_{y_b^c}(y_b^p - y_b^c). \tag{14}$$

Equations (11) and (13) state that the change in AMOC depth in each perturbation run is determined by the specified change in the Southern Ocean surface density ($\Delta\rho_S \propto \Delta S_S^*$), the surface meridional density gradient in the Southern Ocean in the control run (dR_h/dy), the approximately invariant slope of the isopycnal ρ_{bdry} in the Southern Ocean (s), and the simulated changes in the density of the isopycnal boundary $\Delta\rho_{\text{bdry}}$. This applies because $\Delta\rho_{\text{shift}}$, along with the meridional surface density gradient, determines the shift in the outcropping latitude of ρ_{bdry}, which is associated with changes in the AMOC depth through Eq. (7). The approximate invariance of the isopycnal slope is indicated in Fig. 9 and is discussed in section 5c.

We can alternatively characterize the AMOC depth using the vertical density profile in the control run in the South Atlantic, which we define as $R_v(z)$. Under the approximation that the isopycnal slope in the Southern Ocean remains constant, the surface density in the Southern Ocean $R_h(y)$ maps to the deep ocean in the Atlantic basin along isopycnals via

$$R_v(z) = R_h(y_0 - zs). \tag{15}$$

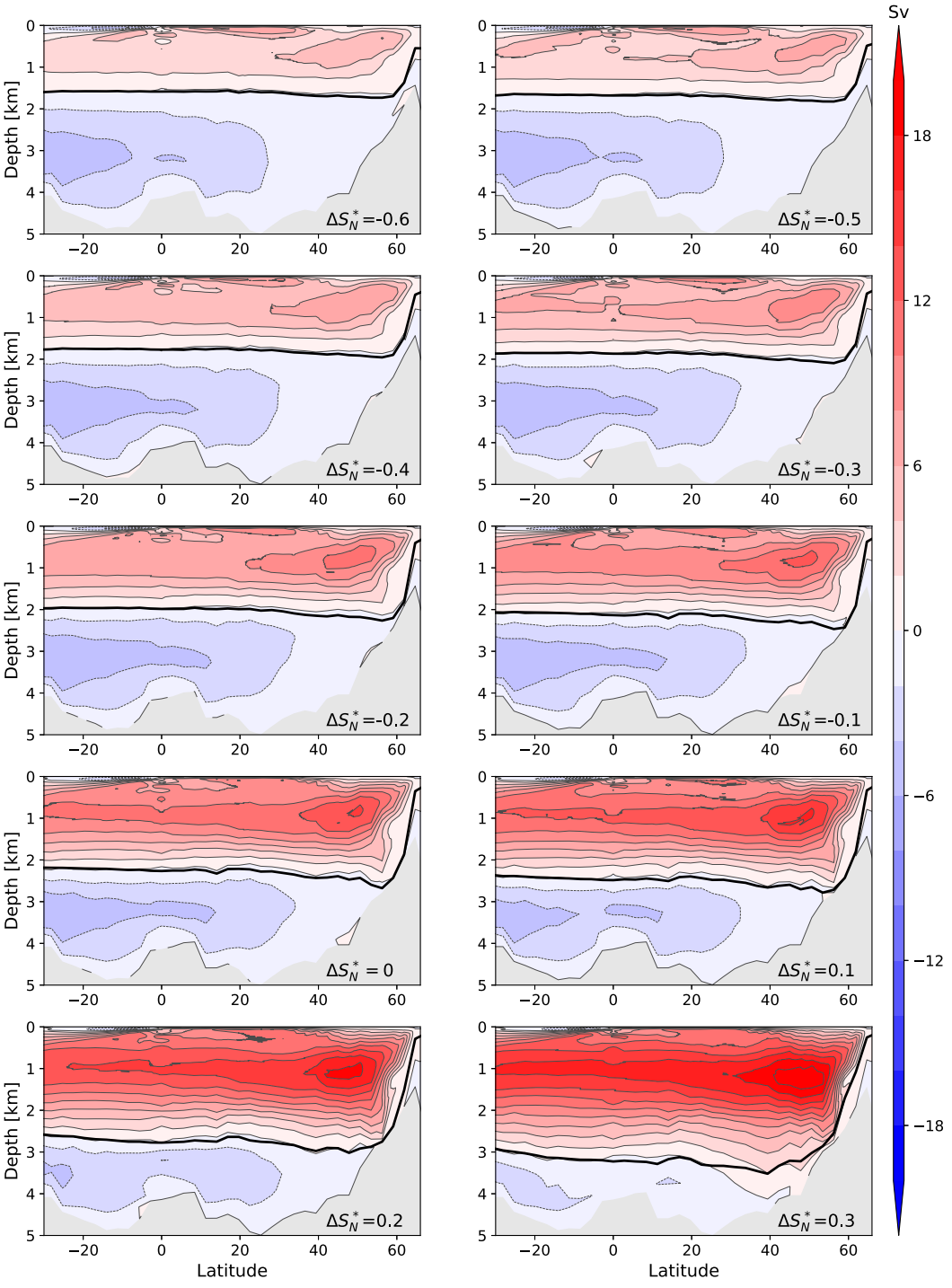

FIG. 8. (a) The AMOC depth [as defined by Eq. (B3)] in the four sets of perturbation runs. The gray dashed line represents the AMOC depth based on predictions of the AMOC depth changes relative to the control run by Eq. (17) using $\Delta\rho_{\text{shift}} = (1/2)\rho_0\beta(\Delta S_N^* - \Delta S_S^*)$. Each error bar represents the depth range among all locations (y) between 30°S and the equator of the zero streamline [$z_{\text{isop}}(y)$] in Eq. (B3). (b) The difference in density between the isopycnal that separates the upper and lower cells and the Southern Ocean perturbation, $\Delta\rho_{\text{shift}} \equiv \Delta\rho_{\text{bdry}} - \Delta\rho_S$, in the four sets of perturbation runs. The gray dashed line represents the equality $\Delta\rho_{\text{shift}} = (1/2)\rho_0\beta(\Delta S_N^* - \Delta S_S^*)$ [Eq. (30)]. In both panels, all of the Symmetric perturbations runs (orange dots) are clumped in a small part of the plot and overlap each other.

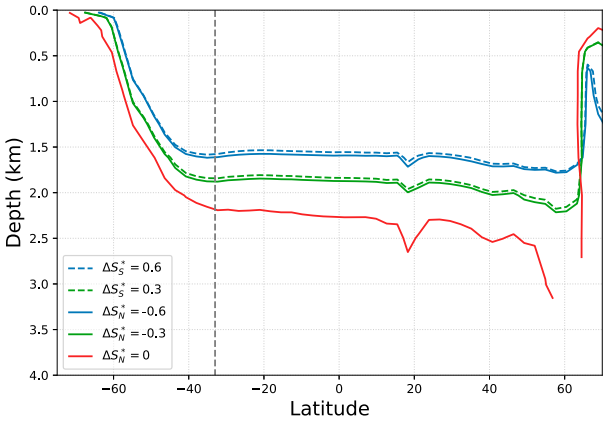

FIG. 9. Contours of the isopycnal that separates the two overturning circulation cells ρ_{bdry}, with potential density zonally averaged in the Atlantic Ocean (north of 33°S) and in the Atlantic sector of the Southern Ocean (south of 33°S) in the Southern Ocean perturbation runs (dashed) and the North Atlantic perturbation runs (solid). Only a subset of the runs is included for clarity. The red line represents the control run, which is equivalent to the North Atlantic perturbation run $\Delta S_N^* = 0$ and the Southern Ocean perturbation run $\Delta S_S^* = 0$. The gray dashed line indicates 33°S.

In perturbation runs with $\Delta S_S^* = 0$, which have approximately the same surface density field in the Southern Ocean as the control run, the vertical density profile in each perturbation run is approximately equivalent to the profile in the control run. In this case, the depth of the isopycnal boundary in a perturbation run ρ^p_{bdry} and the control run ρ^c_{bdry} can be expressed as $R_v^{-1}(\rho^p_{\text{bdry}})$ and $R_v^{-1}(\rho^c_{\text{bdry}})$, respectively, where $R_v^{-1}(\rho) = z$ is the inverse function of the vertical density profile in the control run, which is obtained by averaging the vertical density profile in the Atlantic Ocean between 30°S and the equator. Therefore, the difference in the AMOC depth between the perturbation run and the control run will be

$$\Delta H = R_v^{-1}(\rho^c_{\text{bdry}} + \Delta\rho_{\text{bdry}}) - R_v^{-1}(\rho^c_{\text{bdry}}), \tag{16}$$

noting the definition of $\Delta\rho_{\text{bdry}}$ in Eq. (12) above. The relationship in Eq. (16) is exact for perturbation runs with $\Delta S_S^* = 0$ if the vertical density profile in the South Atlantic remains unchanged from the control run $[R_v(z)]$.

In runs with perturbed Southern Ocean surface density, $\Delta\rho_S \neq 0$, the vertical density profile in the South Atlantic is shifted by approximately $\Delta\rho_S$, Hence we can generalize the expression for the change in AMOC depth to

$$\Delta H = R_v^{-1}(\rho^c_{\text{bdry}} + \Delta\rho_{\text{shift}}) - R_v^{-1}(\rho^c_{\text{bdry}}), \tag{17}$$

noting the definition of $\Delta\rho_{\text{shift}}$ in Eq. (11). Equation (17) assumes that the vertical density profile in the South Atlantic in a given perturbation run shifts by the same amount as the change in the surface density field in the Southern Ocean. It is a more accurate representation than Eq. (13), and the two are equivalent under the additional approximation of constant isopycnal slope in the Southern Ocean.

Next we investigate the dependence of the density of the isopycnal boundary ρ_{bdry} on the surface density perturbations. The final result, which we derive in the remainder of section 4, relates the change in the density ρ_{bdry} and the AMOC depth to the surface density changes in both the North Atlantic and the Southern Ocean.

Because the North Atlantic surface density perturbation ($\Delta\rho_N \equiv \rho_0\beta\Delta S_N^*$) and the Southern Ocean surface density perturbation $\Delta\rho_S$ are the only two independent variables in the idealized perturbation runs, the changes in ρ_{bdry} in the perturbation runs compared with the control run must be expressible as

$$\Delta\rho_{\text{bdry}} = F_1(\Delta\rho_S, \Delta\rho_N), \tag{18}$$

where F_1 is an unknown function. Note that this expression implies that the change in ρ_{bdry} compared with the Southern Ocean surface density perturbation is also a function of the surface density perturbations in the Southern Ocean and the North Atlantic, $\Delta\rho_{\text{shift}} = F_1(\Delta\rho_S, \Delta\rho_N) - \Delta\rho_S$.

Next, we use the perturbation runs to investigate the form of the function $F_1(\Delta\rho_S, \Delta\rho_N)$.

1) SYMMETRIC PERTURBATION RUNS

In the Symmetric perturbation runs, the surface densities in the North Atlantic and the Southern Ocean are perturbed by the same amount, $\Delta\rho_S = \Delta\rho_N$. Because the deep ocean ventilates only in the North Atlantic and the Southern Ocean, this is expected to shift the density uniformly by $\Delta\rho_N$ without any dynamical consequence, with the possible exception of regions close to the ocean surface in the low-latitude Atlantic and in the Indo-Pacific where mixing with the surface water may have some impacts. Therefore, we expect that the changes in ρ_{bdry} will be

$$\Delta\rho_{\text{bdry}} = F_1(\Delta\rho_S, \Delta\rho_S) = \Delta\rho_S, \tag{19}$$

and therefore

$$\Delta\rho_{\text{shift}} = 0 \tag{20}$$

by Eq. (11). This suggests no change in the AMOC depth based on Eq. (13); that is,

$$\Delta H = 0. \tag{21}$$

Indeed, Fig. 7b (cluster of orange dots near origin) confirms that $\Delta\rho_{\text{shift}}$ is approximately zero and Fig. 7a (cluster of orange dots) confirms that the AMOC

depth stays approximately constant in the Symmetric perturbation runs.

2) North Atlantic perturbation runs

In the North Atlantic perturbation runs, $\Delta\rho_S = 0$ and hence $\Delta\rho_{\text{bdry}}$ is a function only of $\Delta\rho_N$. This can be written as

$$\Delta\rho_{\text{bdry}} = F_1(0, \Delta\rho_N) = F_2(\Delta\rho_N), \tag{22}$$

where F_2 is an unknown function that satisfies $F_2(0) = 0$. Since here $\Delta\rho_S = 0$, we have $\Delta\rho_{\text{shift}} = \Delta\rho_{\text{bdry}}$ and hence

$$\Delta\rho_{\text{shift}} = F_2(\Delta\rho_N). \tag{23}$$

3) Southern Ocean perturbation runs

In the Southern Ocean perturbation runs, $\Delta\rho_N = 0$ and hence $\Delta\rho_{\text{bdry}}$ is a function only of $\Delta\rho_S$. The forcing of a given Southern Ocean perturbation run ($\Delta\rho_S$) is equivalent to the sum of a North Atlantic perturbation run with the North Atlantic surface density perturbed by $-\Delta\rho_S$ and a Symmetrical perturbation run with both the North Atlantic and the Southern Ocean surface density perturbed by $\Delta\rho_S$. Approximating that the Symmetric perturbation modifies the density field with no consequence for the AMOC depth, as described above, implies that the change in the density of the isopycnal that separates the two cells in the Southern Ocean perturbation run will be

$$\Delta\rho_{\text{bdry}} = F_1(\Delta\rho_S, 0) = F_2(-\Delta\rho_S) + \Delta\rho_S. \tag{24}$$

This implies that the change in ρ_{bdry} relative to the Southern Ocean surface density perturbation satisfies

$$\Delta\rho_{\text{shift}} = F_2(-\Delta\rho_S) \tag{25}$$

in the Southern Ocean perturbation runs; that is, the AMOC response to a surface density perturbation $\Delta\rho_S$ in the Southern Ocean is equivalent to the AMOC response to a surface density perturbation of opposite sign in the North Atlantic. Figure 7 (cf. red and blue dots) indicates that this equivalence is approximately the case in the model simulations.

4) Antisymmetric perturbation runs

Similar to the Southern Ocean perturbation runs, a given Antisymmetric perturbation run with $\Delta\rho_N = -\Delta\rho_S$ can be approximately decomposed into the sum of a North Atlantic perturbation run with the North Atlantic surface density perturbed by $2\Delta\rho_N$ and a Symmetric perturbation run with both the North Atlantic and the Southern Ocean surface density perturbed by $\Delta\rho_S$. Therefore, we expect the change in the density of the isopycnal boundary $\Delta\rho_{\text{bdry}}$ in the Antisymmetric perturbation runs to be

$$\Delta\rho_{\text{bdry}} = F_2(2\Delta\rho_N) + \Delta\rho_S, \tag{26}$$

with the change in ρ_{bdry} relative to the Southern Ocean surface density perturbation being

$$\Delta\rho_{\text{shift}} = F_2(2\Delta\rho_N); \tag{27}$$

that is, the AMOC response in a given Antisymmetric perturbation with $\Delta\rho_N = -\Delta\rho_S$ is equivalent to a North Atlantic perturbation run with the North Atlantic surface density perturbed by $2\Delta\rho_N$. This relationship can be seen to be approximately the case in the Antisymmetric perturbation runs by comparing the green and blue dots in Fig. 7.

5) Synthesis

Taken together, Eqs. (23), (24), and (27) suggest that $\Delta\rho_{\text{shift}}$ can be expressed as

$$\Delta\rho_{\text{shift}} = F_2(\Delta\rho_N - \Delta\rho_S). \tag{28}$$

In other words, this implies that the change in the potential density of the isopycnal boundary ρ_{bdry} relative to the Southern Ocean surface density perturbation $\Delta\rho_S$ is a function only of the difference between the surface density perturbation in the North Atlantic and the surface density perturbation in the Southern Ocean. This is shown to be the case in the simulation results in Fig. 7b, where $\Delta\rho_{\text{shift}}$ is plotted against $\Delta S_N^* - \Delta S_S^*$ and variations of $\Delta\rho_{\text{shift}}$ in the four sets of idealized perturbation runs approximately fall on a single line.

Therefore, the difference in the AMOC depth between a given perturbation run and the control run can be written from Eq. (13) as

$$\Delta H \approx \frac{s}{(dR_h/dy)|_{y_b^c}} F_2(\Delta\rho_N - \Delta\rho_S). \tag{29}$$

This indicates that changes in the AMOC depth can be attributed to the differences between perturbations to the North Atlantic surface density and the Southern Ocean surface density, which is shown to be the case in the simulation results in Fig. 7a, where the AMOC depth is plotted against $\Delta S_N^* - \Delta S_S^*$ and variations of the AMOC depth in the four sets of idealized perturbation runs fall on a single curve.

We use the results of the perturbation simulations to diagnostically determine the actual form of F_2. The scatterplot of $\Delta\rho_{\text{shift}}$ versus $\Delta S_N^* - \Delta S_S^*$ in Fig. 7b suggests that

$$\Delta\rho_{\text{shift}} = F_2(\Delta\rho_N - \Delta\rho_S) = \frac{1}{2}(\Delta\rho_N - \Delta\rho_S). \tag{30}$$

Combined with the definition of $\Delta\rho_{\text{shift}}$ in Eq. (11), this implies

$$\Delta\rho_{\text{bdry}} = \frac{1}{2}(\Delta\rho_N + \Delta\rho_S), \tag{31}$$

which is a diagnosed result of the idealized perturbation runs.

This indicates that the change in the isopycnal boundary density ρ_{bdry} is given by the average between the change in surface density in the North Atlantic and in the Southern Ocean. This result is in contrast with previous theoretical studies that have assumed ρ_{bdry} to be the maximum surface density in the North Atlantic, and hence that $\Delta\rho_{\text{bdry}}$ depends solely on North Atlantic surface conditions (e.g., Nikurashin and Vallis 2012).

The linear dependence of $\Delta\rho_{\text{bdry}}$ on $\Delta\rho_N$ and $\Delta\rho_S$ would not necessarily have been expected. This diagnosed relationship [Eq. (31)] is obtained based on results from the MITgcm runs with surface forcing based on the CCSM4 PMIP3 PI simulation. In section 5a, we show that this relationship is modified when the deep convection sites move.

Combining Eqs. (17) and (31), along with the vertical density profile $R_v(z)$ in the Atlantic Ocean for the control run, we can predict the variations in the AMOC depth in response to surface density perturbations. This prediction of the geometric model (gray dashed line in Fig. 7a) is shown to be consistent with the perturbation runs. The results imply that the LGM–PI AMOC depth changes simulated in the PMIP3 models can be approximately understood in terms of how the variations in the surface density field compare between the North Atlantic and the Southern Ocean. As illustrated in the schematic (Fig. 10), if the surface density change from the PI to the LGM climate in the Southern Ocean $\Delta\rho_S$ is larger than the North Atlantic $\Delta\rho_N$, the isopycnal boundary ρ_{bdry} that separates the two overturning circulation cells will outcrop in the Southern Ocean at a lower latitude, and thus the AMOC will be shallower at the LGM by ΔH [Eqs. (13), (29), and (17)]. On the other hand, if $\Delta\rho_S$ is smaller than $\Delta\rho_N$, then ρ_{bdry} will outcrop in the Southern Ocean at a higher latitude, and thus the AMOC will be deeper at the LGM.

5. Discussion

a. *What sets the density of the isopycnal boundary between the two overturning circulation cells* ($\Delta\rho_{\text{bdry}}$)*?*

In the MITgcm runs described in section 4a above that have surface forcing from the CCSM4 PMIP3 PI simulation plus a specified perturbation, the convection sites in the North Atlantic and the Southern Ocean do not move substantially in response to the surface density perturbations. The NADW formation in the North Atlantic in the North Atlantic perturbation runs is indicated in Figs. 11a–c. Here we test the extent to which this depends on the reference simulation by carrying out an additional set of MITgcm runs that have surface forcing from the MPI-ESM PMIP3 PI simulation plus the same specified perturbation fields as in the North Atlantic perturbation runs described in section 4a. We find that in these runs, the convection sites shift from the eastern North Atlantic to the south of Greenland in response to the perturbations as ΔS_N^* increases, especially when $\Delta S_N^* > 0$. This is shown in Figs. 11d–f. Whether the convection sites shift in response to a uniform high-latitude perturbation field is expected to depend on factors including the deep ocean stratification in the reference simulation and the strength of the surface perturbation.

Due to the shifted North Atlantic convection sites in the perturbed MPI-ESM simulations, the change in the NADW density is expected to differ from $\Delta\rho_N$ (cf. Fig. 6b), and the diagnostic relationship between ρ_{bdry} and the surface density perturbations in Eq. (31) may be modified. Indeed, we find that when $\Delta S_N^* \geq 0$, the simulated value of $\Delta\rho_{\text{shift}}$ is lower than the value predicted by the diagnostic relationship in Eq. (30) (Fig. 12b). Instead, the isopycnal boundary density $\Delta\rho_{\text{bdry}}$ more closely follows

$$\Delta\rho_{\text{bdry}} = \frac{1}{2}(\Delta\rho_{\text{NADW}} + \Delta\rho_{\text{AABW}}), \tag{32}$$

with ρ_{NADW} and ρ_{AABW} the densities of the NADW and AABW water masses diagnosed from the simulation (cf. Fig. 6). Similarly,

$$\Delta\rho_{\text{shift}} = \frac{1}{2}(\Delta\rho_{\text{NADW}} + \Delta\rho_{\text{AABW}}) - \Delta\rho_S. \tag{33}$$

This change in the expression for $\Delta\rho_{\text{shift}}$ [Eq. (33)] revises the prediction for the changes in the AMOC depth. This is indicated in Fig. 12a as the "corrected predictions." It should be emphasized, however, that unlike the predictions that draw on Eq. (31), these corrected predictions that draw on Eq. (32) require the density of NADW and AABW to be diagnosed from the GCM simulation results (see Fig. 6).

Nonetheless, the shifted North Atlantic convection sites do not change our conclusion that changes in the AMOC depth can be attributed solely to the differences between perturbations to the North Atlantic surface density and perturbations to the Southern Ocean surface density [Eq. (29)]. This is confirmed by comparing the North Atlantic perturbation runs and the Southern Ocean perturbation runs in Fig. 12a, where the AMOC depth changes in these two sets of simulations, plotted against $\Delta S_N^* - \Delta S_S^*$, approximately fall on a single line as in Fig. 7a.

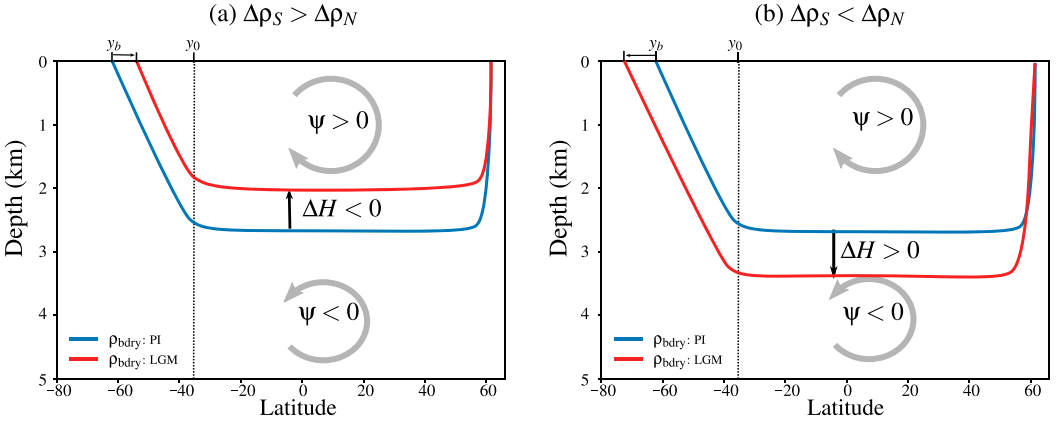

FIG. 10. Schematic diagrams illustrating the proposed connections between the AMOC depth differences between the LGM and PI climates and the surface density changes in the North Atlantic and the Southern Ocean. (a) If the surface density change from the PI to the LGM in the Southern Ocean $\Delta\rho_S$ is larger than in the North Atlantic $\Delta\rho_N$, then the isopycnal boundary ρ_{bdry} that separates the two overturning circulation cells will outcrop in the Southern Ocean at a latitudinal location that is more equatorward by $\Delta H/s$ [Eq. (13)]. Assuming the isopycnal slope remains approximately constant in the Southern Ocean, this means that the AMOC will be shallower by ΔH [Eqs. (29) and (17)] at the LGM. (b) If $\Delta\rho_S$ is smaller than $\Delta\rho_N$, then ρ_{bdry} will outcrop in the Southern Ocean at a location that is more poleward by $\Delta H/s$ and the AMOC will be deeper by ΔH at the LGM. The outcropping position of the isopycnal boundary in the North Atlantic stays at an approximately constant latitude because there is little variation in the latitude of North Atlantic deep convection among most climate models (e.g., Brady et al. 2013, their Fig. 15).

Note that if the the Southern Ocean surface density profile changes by the same amount as ρ_{AABW}, then Eq. (30) is replaced by

$$\Delta\rho_{shift} = \frac{1}{2}(\Delta\rho_{NADW} - \Delta\rho_{AABW}). \tag{34}$$

In this case, the geometric model presented here [Eq. (13)] suggests that the AMOC depth will be correlated with the density difference between the NADW and AABW (e.g., Galbraith and de Lavergne 2019).

The results shown in Fig. 12 imply that the isopycnal boundary that separates the two overturning circulation

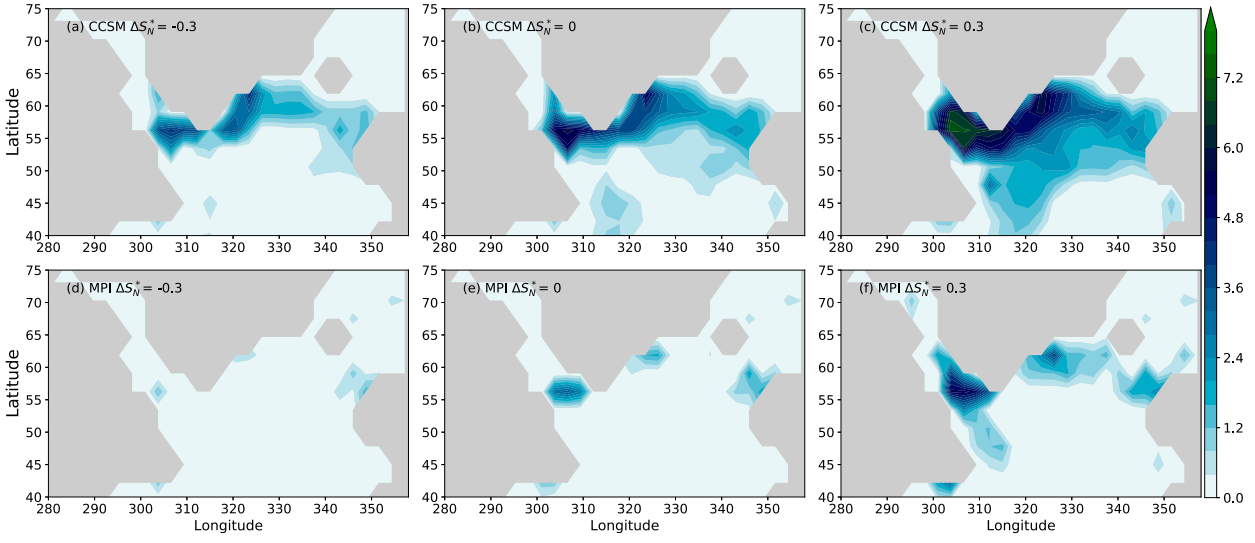

FIG. 11. (a)–(c) Annual-mean frequency of convective adjustments in the North Atlantic perturbation runs described in section 4a, which use the CCSM4 PMIP3 PI run as the reference simulation. (d)–(f) As in (a)–(c), but using the MPI-ESM PMIP3 PI run as the reference simulation. The plotted frequency represents the annual-mean column-integrated number of convective instability events in the MITgcm representation of mixing from static instability, and hence it indicates the horizontal locations of deepwater formation.

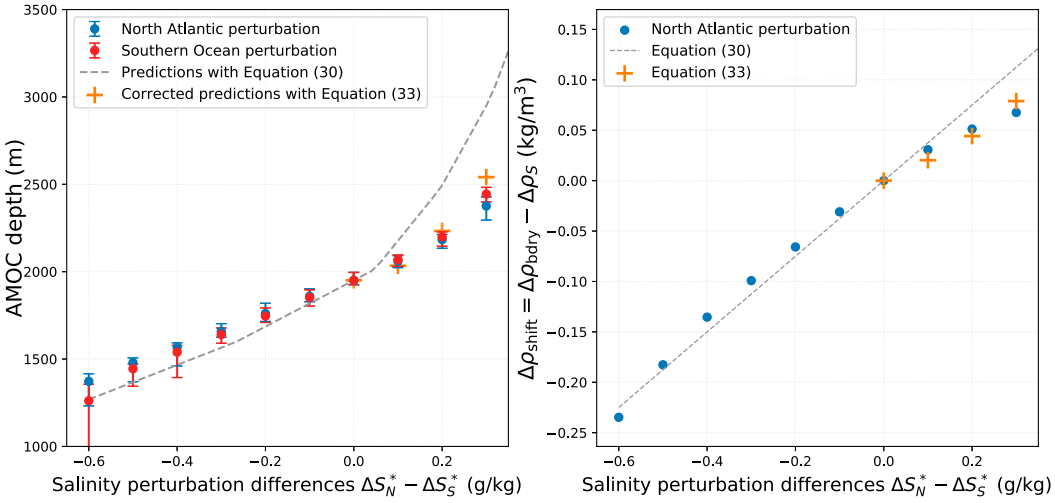

FIG. 12. As in Fig. 7, but using the MPI-ESM PMIP3 PI run as the reference simulation rather than the CCSM4 PMIP3 PI run. Here the corrected predictions for $\Delta S_N^* - \Delta S_S^* \geq 0$ are made using Eq. (33) (orange plus signs), which draw on the density of NADW and AABW diagnosed from the simulations. Only the North Atlantic perturbation runs are plotted in (b).

cells is determined by the densities of the NADW and AABW water masses, and that under a given perturbation, the change in the density of the isopycnal boundary between the two cells is approximately equal to the average of the changes in the densities of the two water masses [Eq. (32)]. This may result from the vertical mixing between the two water masses in the Atlantic Ocean (see Fig. 6a). Given that the isopycnal boundary moves between 1500 and 3000 m (Figs. 7a and 12a), the relationship in Eq. (32) appears to be relatively insensitive to the value of the diapycnal diffusivity (see Figs. 7b and 12b), which varies in this configuration of MITgcm from $3 \times 10^{-5}\,\mathrm{m^2\,s^{-1}}$ at the surface to $1.3 \times 10^{-4}\,\mathrm{m^2\,s^{-1}}$ below 2000-m depth.

The finding here that the density of the isopycnal separating the two cells (ρ_{bdry}) is related to both North Atlantic and Southern Ocean conditions [Eq. (32)] is in contrast with previous theoretical studies that explicitly or implicitly assume that ρ_{bdry} is the maximum surface density in the North Atlantic (e.g., Nikurashin and Vallis 2012; Ferrari et al. 2014; Thompson et al. 2016), which would imply $\Delta\rho_{\mathrm{bdry}} = \Delta\rho_{\mathrm{NADW}}$. This previous assumption was based on a simplified viewpoint of the overturning circulation that ignored the temporal and longitudinal variations of the density fields, in which case only isopycnals above ρ_{bdry} could outcrop in both the Southern Ocean and the North Atlantic (e.g., Nikurashin and Vallis 2012). In a more realistic setup, water masses below ρ_{bdry} can also outcrop in the North Atlantic even though their isopycnals do not outcrop in the time-mean zonally integrated overturning circulation streamfunction.

b. *Comparison with previous studies*

Previous studies have differed on whether the surface of the North Atlantic or the Southern Ocean dictates the depth of the boundary between the upper and lower ocean circulation cells. The present study suggests that it is both.

The geometric model developed in section 4 relies on the spatial uniformity of the high-latitude surface density differences in the idealized perturbation runs, where the deep ocean stratification stays approximately constant, and cannot be directly applied to other more realistic GCM simulations. Inspired by Fig. 6a and Eq. (32), we can approximate the potential density of the isopycnal boundary separating the two overturning circulation cells as

$$\rho_{\mathrm{bdry}} \approx \rho'_{\mathrm{bdry}} \equiv \frac{1}{2}(\rho_{\mathrm{NATL}} + \rho_{\mathrm{SO}}), \tag{35}$$

where ρ_{NATL}, an approximation to ρ_{NADW}, is the maximum zonal-mean wintertime surface density in the subpolar North Atlantic, and ρ_{SO}, an approximation to ρ_{AABW}, is the maximum zonal-mean surface density in the Southern Ocean. We use ρ'_{bdry} instead of ρ_{bdry} to indicate that this is an approximation.

According to the geometric model (Fig. 10), the shift in the outcropping latitude of the isopycnal ρ'_{bdry} in the Southern Ocean is expected to explain the change in the AMOC depth changes between simulations of the PI and LGM climates. Indeed, in Fig. 13e we show that the shift in the outcropping latitude of the predicted isopycnal boundary ρ'_{bdry} is approximately consistent with

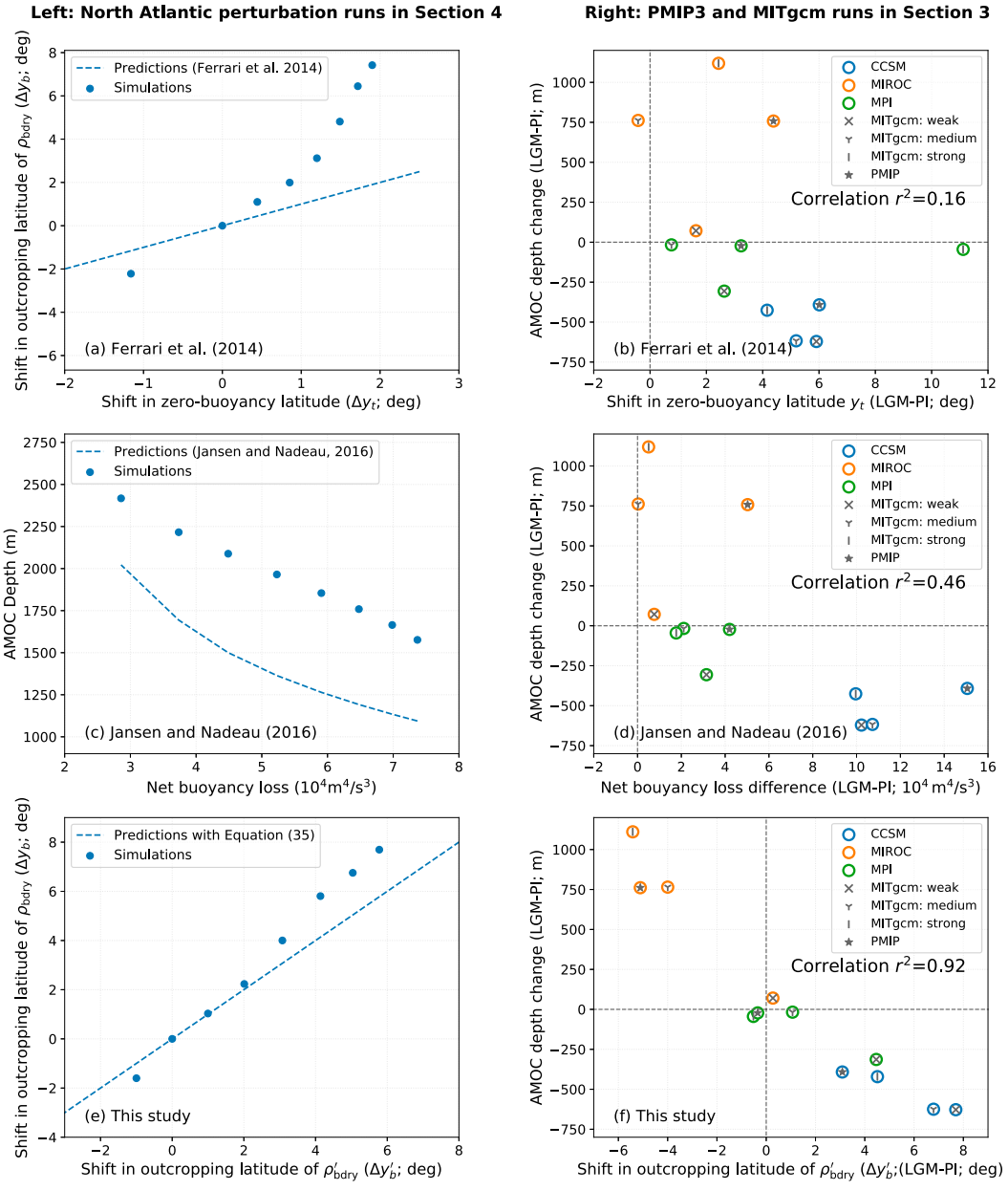

FIG. 13. Comparison of this study with previous theories for the AMOC depth. (a) Shift in the outcropping latitude of the isopycnal boundary ρ_{bdry} (y_b) vs the shift in transition latitude (y_t) of the zonal-mean surface buoyancy flux in the Southern Ocean. (b) Change in the AMOC depth between the simulated PI and LGM climates vs the shift in the transition latitude y_t of the zonal-mean surface buoyancy flux in the Southern Ocean. (c) AMOC depth vs the net surface buoyancy loss in southern high latitudes (see section 5b for details). (d) As in (b), but with the change in net surface buoyancy loss between the simulated PI and LGM climates plotted on the horizontal axis. (e) The shift in the outcropping latitude of the isopycnal boundary ρ_{bdry} vs the shift in the outcropping latitude of the isopycnal ρ'_{bdry}, which is defined in Eq. (35). (f) As in (b), but with the shift in the outcropping latitude of the isopycnal ρ'_{bdry} between the simulated PI and LGM climates plotted on the horizontal axis.

the shift in the outcropping latitude of the actual simulated isopycnal boundary ρ_{bdry} in the perturbation runs, and in Fig. 13f we show that it explains over 90% of the variance in the simulated AMOC depth differences between the PI and LGM climates among the PMIP3 simulations and the MITgcm ocean-only runs described in section 3. The similar behavior between the PMIP3 simulations and the MITgcm ocean-only runs also

suggests that the potential lack of equilibrium in the coupled PMIP3 simulations does not contribute substantially to the intermodel spread of the simulated LGM–PI AMOC depth difference (cf. Marzocchi and Jansen 2017).

Next, we compare the framework developed in the present study with the implications of two previous influential theoretical studies that each proposed a separate relationship between the Southern Ocean surface buoyancy forcing and the AMOC depth.

1) FERRARI ET AL. (2014)

Ferrari et al. (2014) approximate the circulation in the Southern Ocean to be adiabatic, and based on this and several other assumptions they propose that the AMOC depth is determined by the transition latitude y_t where the Southern Ocean surface buoyancy flux changes sign. Here we test this idea using the simulations described in the present study.

In response to surface density changes in the North Atlantic perturbation runs, the overturning circulation varies in the Southern Ocean, and there are changes in the Southern Ocean surface buoyancy forcing associated with this due to the surface temperature and salinity being relaxed toward specified values. As a result, the transition latitude y_t of the diagnosed Southern Ocean surface buoyancy flux shifts in response to the surface perturbations (Fig. 13a).

Ferrari et al. (2014) posited that the isopycnal boundary ρ_{bdry} outcrops at y_t. However, we find that the shift in the transitional latitude y_t differs substantially from the outcropping latitude of the isopycnal boundary ρ_{bdry} (Fig. 13a). We find that the AMOC depth is not closely related to y_t, with the shift in the transition latitude y_t explaining only 16% of the variance in simulated AMOC depth differences between the PI and LGM climates among the PMIP3 simulations and the MITgcm ocean-only runs described in section 3. Previous work (Sun et al. 2018) used CESM ocean-only simulations to attribute the discrepancy between the Southern Ocean surface buoyancy flux and the AMOC depth to diapycnal processes in the Southern Ocean, which were neglected in Ferrari et al. (2014).

2) JANSEN AND NADEAU (2016)

Jansen and Nadeau (2016) used idealized model simulations with a single basin that represents the Atlantic Ocean to suggest that the rate of surface buoyancy loss across the Southern Ocean determines the AMOC depth. This was based on the approximation that the total surface buoyancy loss in the Southern Ocean is balanced by the interior buoyancy gain due to diapycnal mixing across the boundary between the upper and lower overturning circulation cells outside the Southern Ocean, which can be written as

$$B = \iint \kappa \frac{\partial}{\partial z} b(x, y, H')\, dx\, dy. \tag{36}$$

Here B is buoyancy loss integrated over all ocean locations to the south of 60°S and hence is expected to include most of the negative buoyancy flux associated with deepwater formation in the Southern Ocean, $b(x, y, z)$ represents three-dimensional buoyancy field $[b \equiv -g(\rho - \rho_0)/\rho_0]$, H' is the depth where the above buoyancy balance is achieved, and the integration on the right-hand side is performed on the constant depth level H' over all locations to the north of 30°S. Jansen and Nadeau (2016) identify H' as the depth of the bottom of the AMOC cell. We examined the extent to which H' can be used to predict the AMOC depth in the simulation results.

In the North Atlantic perturbation runs as well as the Southern Ocean perturbation runs, the deep ocean stratification remains approximately the same as in the control run, which is expected since the perturbations in the Southern Ocean are spatially uniform. Thus, H' can be calculated by inverting the vertical profile of the integrated interior diapycnal buoyancy flux simulated in the Atlantic and Indo-Pacific basins. We find that the depth H' where the buoyancy balance in Eq. (36) applies is substantially shallower in the perturbation simulations than the actual simulated AMOC depth (Fig. 13c).

This difference between H' and the actual AMOC depth may be due to diabatic processes in the Southern Ocean that are neglected in Eq. (36). By neglecting diabatic processes in the Southern Ocean, especially in the surface mixed layer (cf. Marshall et al. 1999), the interior buoyancy gain across the overturning circulation cell boundary is overestimated. The integrated interior diapycnal fluxes support the interior diapycnal transformation of water masses and increase upward in MITgcm (cf. Munk 1966), which may explain why the estimated depth H' is shallower than the actual AMOC depth. The difference between H' and the actual AMOC depth is hence expected to depend on the amount of diapycnal mixing in the Southern Ocean, which is a function of the density stratification. In the perturbation runs, which all have approximately the same deep ocean stratification, this difference is fairly uniform (Fig. 13c) such that changes in the AMOC depth between simulations are approximately consistent with changes in H'. However, the deep ocean stratification varies among the PMIP3 simulations and the MITgcm ocean-only runs described in section 3. Consequently, the difference between H' and the simulated AMOC depth is not uniform in these runs. Consistent with this, we find that changes in the surface buoyancy forcing in the Southern Ocean have

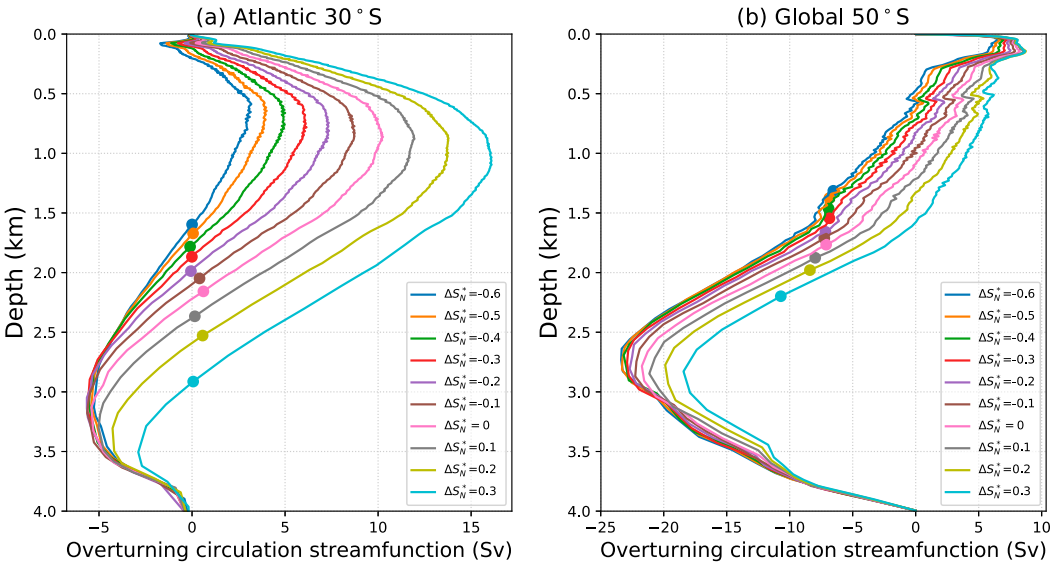

FIG. 14. The isopycnal overturning circulation streamfunction in the North Atlantic perturbation runs at (a) 30°S in the Atlantic basin and (b) 50°S in the Southern Ocean. The overturning circulation streamfunction in the Southern Ocean is calculated according to Eq. (B1) with the zonal integral expanded to include all longitudes around the globe. The dots represent the depth of the ρ_{bdry} isopycnal. Note that the dots in (b) do not closely correspond with the depth where the streamfunction is zero because the depth of the ρ_{bdry} isopycnal is defined as the average between 30°S and the equator in the Atlantic Ocean.

only limited ability to explain the changes in the AMOC depth among the simulations plotted in Fig. 13d (correlation of $r^2 = 0.46$).

c. *Isopycnal slope*

Varations of the isopycnal slope in response to surface perturbations in simulations that use a single-basin model with a flat bottom (e.g., Wolfe and Cessi 2014) tend to be larger than in the MITgcm simulations presented here. In these single-basin models, the contributions to the Southern Ocean overturning circulation due to standing eddies are minimal (e.g., Wolfe and Cessi 2014, their Fig. 13), and the isopycnal slope can be connected to the Southern Ocean overturning circulation through residual-mean theory using (Marshall and Radko 2003)

$$\psi = \frac{\tau_x L_x}{\rho_0 f} + K_{\text{GM}} s L_x, \tag{37}$$

where τ_x represents the zonally averaged zonal wind stress forcing, L_x is the length of a latitude circle in the Southern Ocean, K_{GM} is the GM thickness diffusivity, and f is the Coriolis parameter. Note that the second term ($K_{\text{GM}} s L_x$) is a representation of the transient eddies. Based on this relationship, the isopycnal slope in the North Atlantic perturbation runs would be expected to become smaller in order to balance the more positive Southern Ocean overturning circulation streamfunction (Fig. 14).

However, the MITgcm simulations in this study have a more realistic setup with two basins and a bottom that is not flat, and in these simulations standing eddies can contribute a substantial component to the Southern Ocean overturning circulation (e.g., Tréguier et al. 2007; Ballarotta et al. 2013). Therefore, changes in the Southern Ocean residual-mean overturning circulation can be balanced by an enhancement of the standing eddy contributions, which are not represented in Eq. (37), thereby allowing the isopycnal slope to stay approximately constant.

Additionally, the Southern Ocean overturning circulation streamfunction associated with the isopycnal ρ_{bdry} is approximately constant in the North Atlantic perturbation runs, especially for $\Delta S_N^* < 0.3$ (Fig. 14b). This approximately constant streamfunction associated with ρ_{bdry} reflects a similar contribution from the Indo-Pacific Ocean among the idealized perturbation runs, which in turn is due to the approximately constant deep ocean stratificaiton in the Indo-Pacific basin [Eq. (15)]. This, together with the standing eddies, contributes to the approximately constant slope of the isopycnal contour ρ_{bdry} in the idealized perturbation runs (Fig. 9).

In the PMIP3 coupled simulations, the Southern Ocean surface forcing differs between the PI and LGM climates. Hence the isopycnal slope may experience larger changes in the PMIP3 coupled simulations than in the idealized perturbation runs. Here we estimate how

much the isopycnal slope changes contribute to the LGM–PI AMOC depth difference in the PMIP3 coupled simulations. Using the approximate isopycnal slope of −1000 m per degree estimated from the CCSM4 PMIP3 PI simulation, the 3° northward shift in the outcropping latitude of the isopycnal boundary from the PI to LGM climate (Fig. 13f) indicates a shoaling of 300 m, which explains approximately 77% of the LGM–PI AMOC depth changes in CCSM4, with the remaining 90 m related to changes in the isopycnal slope changes. Similarly, we estimate that the isopycnal slope changes only contribute 30% of the LGM–PI depth difference in MIROC-ESM. This suggests that the approximation of a constant isopycnal slope may also be plausible for the PMIP3 coupled simulations.

d. Nordic seas

In the MITgcm simulations of the present study, NADW is formed exclusively in the subpolar North Atlantic. This is consistent with previous climate model studies that have emphasized the impact of the subpolar North Atlantic on the AMOC (e.g., Yeager and Danabasoglu 2014). However, recent observations suggest that the southward branch of the AMOC originates mainly from the Nordic seas overflows, rather than from deep convection in the subpolar North Atlantic (Lozier et al. 2019).

At the LGM, sea ice in the Northern Hemisphere has been suggested to have covered the Nordic seas, thereby reducing the heat loss from the ocean to the atmosphere in these regions (e.g., Brady et al. 2013, their Fig. 10) and forming a fresh layer at the surface (e.g., Dokken et al. 2013). This may imply substantially different deep convection sites in the North Atlantic and may have caused a decrease in the NADW density at the LGM, which may plausibly have contributed to shoaling of the AMOC. The lack of representation of such processes is a caveat of the present study.

6. Summary

Paleoclimate proxy data suggest that the AMOC was approximately 1000 m shallower at the LGM compared with the current climate (e.g., Lund et al. 2011). Some previous studies have connected this change to variations in surface buoyancy forcing in the Southern Ocean (Ferrari et al. 2014; Jansen and Nadeau 2016), whereas others have instead connected it to surface conditions in the North Atlantic (e.g., Muglia and Schmittner 2015; Oka et al. 2012). A concerted effort to simulate the LGM climate in comprehensive models (PMIP3) has yielded widely varied results for the LGM–PI difference in AMOC depth, with the majority of models simulating a deeper and stronger AMOC at the LGM (e.g., Muglia and Schmittner 2015). The causes for this intermodel spread and for the discrepancy between the model simulations and proxy reconstructions have remained unresolved.

The present study examines the simulated surface density field and AMOC depth in the PMIP3 simulations of the PI and LGM climates. Based on the findings presented here, we suggest that the changes in the AMOC depth are directly connected to changes in the surface density fields in both the North Atlantic and the Southern Ocean. We demonstrate this using simulations with an ocean-only model with varying restoring strengths in the surface forcing.

Next, using a series of ocean-only model simulations that have idealized perturbations to the surface salinity field, in concert with a geometric model of the overturning circulation, we propose a way to quantify the connection between the AMOC depth and the simulated surface density field in both the North Atlantic and the Southern Ocean [Eqs. (13) and (34)]. The resulting theory predicts AMOC depth changes between different simulated climates based on the change in the densities of NADW and AABW waters, as well as the surface density distribution and isopycnal slope in the Southern Ocean.

Hence the viewpoint proposed in this study allows a two-step process for identifying the AMOC depth. First, a potential density representing the average between NADW and AABW is selected. Next, assuming that the isopycnal of this density has a constant slope in the Southern Ocean and is horizontal elsewhere, the depth of this isopycnal outside the Southern Ocean is identified using the isopycnal slope and its outcropping latitude in the Southern Ocean. This represents the AMOC depth, which is defined here as the depth of the boundary between the upper and lower overturning circulation cells. We show that this method provides an accurate estimate of the change in AMOC depth between the LGM and PI simulations in a range of different models and surface forcing fields. The viewpoint presented here sheds light on how changes in surface forcing in both the North Atlantic and the Southern Ocean influence the AMOC depth changes between two climate states.

We note that the geometric model proposed in this study is a diagnostic tool that connects the AMOC depth to the surface density field, which is strongly coupled to the atmospheric and oceanic circulation. There are additionally a number of caveats that should accompany these results. This study focuses on models, which offer an incomplete picture of the real world. Furthermore, the coarse-resolution ocean-only simulations do not resolve eddies, which have been suggested

to be important for the response of the Southern Ocean circulation to surface perturbations (e.g., Munday et al. 2013). The model also does not resolve coastal processes in the North Atlantic and the Southern Ocean, which have been suggested to be important for the formation of NADW and AABW (e.g., Snow et al. 2016).

In conclusion, the results in this study highlight the close connection of the simulated surface density in both the North Atlantic and the Southern Ocean to the depth of the AMOC. This implies that any process that affects the density of NADW, the density of the AABW, or the Southern Ocean surface density distribution should be expected to influence the AMOC depth. Such processes may include surface buoyancy forcing, wind stress forcing, and mixed layer processes in both high-latitude and low-latitude regions.

Acknowledgments. Without implying their endorsement, we thank Paola Cessi, Lynne Talley, Shang-Ping Xie, and Andrew Thompson for helpful discussions. S.S. and I.E. are supported by National Science Foundation Grant OPP-1643445. A.L.S. is supported by the National Science Foundation under Grants ANT-1543388 and OCE-1751386.

APPENDIX A

Varying the Restoring Time Scales

Here we discuss the impacts of varying the restoring time scales on the reproduction of the PMIP3 surface density and surface buoyancy flux in the ocean-only simulations. The equations for temperature and salinity at the sea surface in MITgcm can be written as

$$\frac{\partial \theta}{\partial t} = \frac{F_\theta}{\rho_0 c_p h_s} + \chi_\theta, \tag{A1a}$$

$$\frac{\partial S}{\partial t} = \frac{S_o F_{\text{salt}}}{h_s} + \chi_{\text{salt}}, \tag{A1b}$$

where χ represents the advection and diffusion terms in the temperature and salinity equations for the MITgcm simulations. Thus, the evolution of temperature and salinity is determined by surface buoyancy conditions (first term) and ocean processes (second term). Similarly, the temperature and salinity at sea surface in the PMIP3 simulations can be written as

$$\frac{\partial \theta^*}{\partial t} = \frac{F^*_\theta}{\rho_0 c_p h_s} + \chi^*_\theta, \tag{A2a}$$

$$\frac{\partial S^*}{\partial t} = \frac{S_0}{h_s} F^*_{\text{salt}} + \chi^*_{\text{salt}}, \tag{A2b}$$

where χ^* represents the climatological monthly-mean advection and diffusion terms in the temperature and salinity equations for the PMIP3 simulations.

a. Strong relaxation

In the limit of strong relaxation ($\tau_\theta \to 0$ and $\tau_{\text{salt}} \to 0$), the dominant balance in Eq. (4) is between the relaxation terms, implying

$$\theta = \theta^*, \tag{A3a}$$

$$S = S^*. \tag{A3b}$$

Combining Eq. (A3) with Eqs. (A1) and (A2) leads to

$$F_\theta - F^*_\theta = \rho_0 c_p h_s (\chi^*_\theta - \chi_\theta), \tag{A4a}$$

$$F_{\text{salt}} - F^*_{\text{salt}} = \frac{h_s}{S_o}(\chi^*_{\text{salt}} - \chi_{\text{salt}}). \tag{A4b}$$

Therefore, using the surface buoyancy boundary conditions in Eq. (4) in the limit of strong relaxation, the surface density field of the PMIP3 simulation will be reproduced in MITgcm, but the surface buoyancy flux in MITgcm would differ from the PMIP3 simulation due to their different representations of ocean dynamics.

b. Weak relaxation

In the limit of weak relaxation ($\tau_\theta \to \infty$ and $\tau_{\text{salt}} \to \infty$), on the other hand, the relaxation terms in Eq. (4) can be neglected, implying

$$F_\theta = F^*_\theta, \tag{A5a}$$

$$F_{\text{salt}} = F^*_{\text{salt}}. \tag{A5b}$$

Combining Eq. (A5a) with Eqs. (A1) and (A2) leads to

$$\theta - \theta^* = \int (\chi_\theta - \chi^*_\theta)\, dt, \tag{A6a}$$

$$S - S^* = \int (\chi_{\text{salt}} - \chi^*_{\text{salt}})\, dt. \tag{A6b}$$

Therefore, using the surface buoyancy boundary conditions in Eq. (4) in the limit of weak relaxation, the surface buoyancy flux in the PMIP3 simulation would be reproduced in MITgcm, but the simulated surface density in MITgcm would differ from the PMIP3 simulation due to their different representation of ocean dynamics.

This highlights a trade-off that depends on the surface relaxation time scale between reproduction of the

PMIP3 surface density and reproduction of the PMIP3 surface buoyancy flux in the MITgcm simulations. In the conceptual model analyzed in this appendix, the former is better reproduced with shorter time scales (i.e., stronger relaxation), whereas the latter is better reproduced with longer time scales (i.e., weaker relaxation). Figure 3 illustrates that the same qualitative behavior occurs in the MITgcm simulations presented in this study. This suggests that by varying the restoring time scales in the MITgcm simulations, we can investigate the relative importance of the surface density distribution versus the surface buoyancy flux distribution in setting the AMOC depth, as is done in section 3 of the main text.

APPENDIX B

Definition of the AMOC Depth Based on Isopycnal Overturning Circulation

We calculate the isopycnal overturning circulation streamfunction on σ_2 coordinates (where σ_2 is the potential density referenced to 2000 dbar) as

$$\psi(y,\sigma_2) = -\frac{1}{T}\int_0^T\int_{x_w}^{x_e}\int_{z_{\rm bot}}^0 v_r(x,y,z,t)\,\mathscr{H}[\sigma_2'(x,y,z,t)-\sigma_2]\,dz\,dx\,dt, \tag{B1}$$

where $T = 100$ years is the averaging period, $\mathscr{H}$ is the Heaviside step function, v_r is the total meridional velocity that includes both the Eulerian-mean flow and the eddy-bolus contribution due to the parameterized eddies, and σ_2' is the σ_2 field calculated by the model at each location. The isopycnal overturning circulation streamfunction ψ is then mapped to depth coordinates using the mean depth of each isopycnal. Following Nurser and Lee (2004), we define the mean depth of a given isopycnal $\hat{z}(y, \sigma_2)$ implicitly via

$$\int_{x_w}^{x_e}\int_{z_{\rm bot}}^{\hat{z}(y,\sigma_2)} dx\,dz = \frac{1}{T}\int_0^T\int_{x_w}^{x_e}\int_{z_{\rm bot}}^0 \mathscr{H}[\sigma_2(x,y,z,t)-\sigma_2']\,dx\,dz\,dt, \tag{B2}$$

such that the cross-sectional area below $\hat{z}$ at latitude y is equal to the cross-sectional area of fluid denser than σ_2. For the Atlantic Ocean, the zonal integration in Eqs. (B1) and (B2) is from the western boundary x_w to the eastern boundary x_e of the basin. The resulting AMOC streamfunction $\psi_{\rm atl}$ for each North Atlantic perturbation simulation is plotted in Fig. 8. For the Southern Ocean, the zonal integration is around the globe.

Similar to Eq. (2), we define the AMOC depth as the depth of the zero contour of ψ averaged between 30°S and the equator, that is,

$$H_{\rm isop} = -\frac{1}{L_y}\int_{-L_y}^0 z_{\rm isop}(y)\,dy, \tag{B3}$$

where $z_{\rm isop}$ is the depth of the streamline $\psi = 0$ at meridional location y such that

$$\psi[y,\sigma_2(y,z_{\rm isop})] = 0. \tag{B4}$$

REFERENCES

Ballarotta, M., S. Drijfhout, T. Kuhlbrodt, and K. Döös, 2013: The residual circulation of the Southern Ocean: Which spatio-temporal scales are needed? *Ocean Modell.*, **64**, 46–55, https://doi.org/10.1016/j.ocemod.2013.01.005.

Böning, C. W., A. Dispert, M. Visbeck, S. Rintoul, and F. U. Schwarzkopf, 2008: The response of the Antarctic Circumpolar Current to recent climate change. *Nat. Geosci.*, **1**, 864–869, https://doi.org/10.1038/ngeo362.

Braconnot, P., S. P. Harrison, M. Kageyama, P. J. Bartlein, V. Masson-Delmotte, A. Abe-Ouchi, B. Otto-Bliesner, and Y. Zhao, 2012: Evaluation of climate models using palaeoclimatic data. *Nat. Climate Change*, **2**, 417–424, https://doi.org/10.1038/nclimate1456.

Brady, E. C., B. L. Otto-Bliesner, J. E. Kay, and N. Rosenbloom, 2013: Sensitivity to glacial forcing in the CCSM4. *J. Climate*, **26**, 1901–1925, https://doi.org/10.1175/JCLI-D-11-00416.1.

Bryan, K., 1984: Accelerating the convergence to equilibrium of ocean-climate models. *J. Phys. Oceanogr.*, **14**, 666–673, https://doi.org/10.1175/1520-0485(1984)014<0666:ATCTEO>2.0.CO;2.

——, and L. Lewis, 1979: A water mass model of the World Ocean. *J. Geophys. Res.*, **84**, 2503–2517, https://doi.org/10.1029/JC084iC05p02503.

Cessi, P., 2018: The effect of Northern Hemisphere winds on the meridional overturning circulation and stratification. *J. Phys. Oceanogr.*, **48**, 2495–2506, https://doi.org/10.1175/JPO-D-18-0085.1.

Danabasoglu, G., J. C. McWilliams, and W. G. Large, 1996: Approach to equilibrium in accelerated global oceanic models. *J. Climate*, **9**, 1092–1110, https://doi.org/10.1175/1520-0442(1996)009<1092:ATEIAG>2.0.CO;2.

——, W. G. Large, and B. P. Briegleb, 2010: Climate impacts of parameterized Nordic Sea overflows. *J. Geophys. Res.*, **115**, C11005, https://doi.org/10.1029/2010JC006243.

——, S. C. Bates, B. P. Briegleb, S. R. Jayne, M. Jochum, W. G. Large, S. Peacock, and S. G. Yeager, 2012: The CCSM4 ocean component. *J. Climate*, **25**, 1361–1389, https://doi.org/10.1175/JCLI-D-11-00091.1.

Dokken, T. M., K. H. Nisancioglu, C. Li, D. S. Battisti, and C. Kissel, 2013: Dansgaard-Oeschger cycles: Interactions between ocean and sea ice intrinsic to the Nordic seas. *Paleoceanography*, **28**, 491–502, https://doi.org/10.1002/palo.20042.

Exarchou, E., T. Kuhlbrodt, J. M. Gregory, and R. S. Smith, 2015: Ocean heat uptake processes: A model intercomparison. *J. Climate*, **28**, 887–908, https://doi.org/10.1175/JCLI-D-14-00235.1.

Ferrari, R., M. F. Jansen, J. F. Adkins, A. Burke, A. L. Stewart, and A. F. Thompson, 2014: Antarctic sea ice control on ocean circulation in present and glacial climates. *Proc. Natl. Acad. Sci. USA*, **111**, 8753–8758, https://doi.org/10.1073/pnas.1323922111.

Galbraith, E., and C. de Lavergne, 2019: Response of a comprehensive climate model to a broad range of external forcings: Relevance for deep ocean ventilation and the development of late Cenozoic ice ages. *Climate Dyn.*, **52**, 653–679, https://doi.org/10.1007/S00382-018-4157-8.

Gebbie, G., 2014: How much did glacial North Atlantic water shoal? *Paleoceanography*, **29**, 190–209, https://doi.org/10.1002/2013PA002557.

Gent, P. R., and G. Danabasoglu, 2011: Response to increasing Southern Hemisphere winds in CCSM4. *J. Climate*, **24**, 4992–4998, https://doi.org/10.1175/JCLI-D-10-05011.1.

Gnanadesikan, A., 1999: A simple predictive model for the structure of the oceanic pycnocline. *Science*, **283**, 2077–2079, https://doi.org/10.1126/science.283.5410.2077.

Griffies, S. M., 1998: The Gent–McWilliams skew flux. *J. Phys. Oceanogr.*, **28**, 831–841, https://doi.org/10.1175/1520-0485(1998)028<0831:TGMSF>2.0.CO;2.

Hain, M. P., D. M. Sigman, and G. H. Haug, 2010: Carbon dioxide effects of Antarctic stratification, North Atlantic intermediate water formation, and subantarctic nutrient drawdown during the last ice age: Diagnosis and synthesis in a geochemical box model. *Global Biogeochem. Cycles*, **24**, GB4023, https://doi.org/10.1029/2010GB003790.

Haney, R. L., 1971: Surface thermal boundary condition for ocean circulation models. *J. Phys. Oceanogr.*, **1**, 241–248, https://doi.org/10.1175/1520-0485(1971)001<0241:STBCFO>2.0.CO;2.

Huber, M. B., and L. Zanna, 2017: Drivers of uncertainty in simulated ocean circulation and heat uptake. *Geophys. Res. Lett.*, **44**, 1402–1413, https://doi.org/10.1002/2016GL071587.

Jackett, D. R., and T. J. McDougall, 1995: Minimal adjustment of hydrographic profiles to achieve static stability. *J. Atmos. Oceanic Technol.*, **12**, 381–389, https://doi.org/10.1175/1520-0426(1995)012<0381:MAOHPT>2.0.CO;2.

Jansen, M. F., and L.-P. Nadeau, 2016: The effect of Southern Ocean surface buoyancy loss on the deep ocean circulation and stratification. *J. Phys. Oceanogr.*, **46**, 3455–3470, https://doi.org/10.1175/JPO-D-16-0084.1.

Karsten, R. H., and J. Marshall, 2002: Constructing the residual circulation of the ACC from observations. *J. Phys. Oceanogr.*, **32**, 3315–3327, https://doi.org/10.1175/1520-0485(2002)032<3315:CTRCOT>2.0.CO;2.

Klockmann, M., U. Mikolajewicz, and J. Marotzke, 2018: Two AMOC states in response to decreasing greenhouse gas concentrations in the coupled climate model MPI-ESM. *J. Climate*, **31**, 7969–7984, https://doi.org/10.1175/JCLI-D-17-0859.1.

Lozier, M. S., 2012: Overturning in the North Atlantic. *Annu. Rev. Mar. Sci.*, **4**, 291–315, https://doi.org/10.1146/annurev-marine-120710-100740.

——, and Coauthors, 2019: A sea change in our view of overturning in the subpolar North Atlantic. *Science*, **363**, 516–521, https://doi.org/10.1126/science.aau6592.

Lumpkin, R., and K. Speer, 2007: Global ocean meridional overturning. *J. Phys. Oceanogr.*, **37**, 2550–2562, https://doi.org/10.1175/JPO3130.1.

Lund, D., J. Adkins, and R. Ferrari, 2011: Abyssal Atlantic circulation during the Last Glacial Maximum: Constraining the ratio between transport and vertical mixing. *Paleoceanography*, **26**, PA1213, https://doi.org/10.1029/2010PA001938.

Marshall, D. P., and L. Zanna, 2014: A conceptual model of ocean heat uptake under climate change. *J. Climate*, **27**, 8444–8465, https://doi.org/10.1175/JCLI-D-13-00344.1.

Marshall, J., and T. Radko, 2003: Residual-mean solutions for the Antarctic Circumpolar Current and its associated overturning circulation. *J. Phys. Oceanogr.*, **33**, 2341–2354, https://doi.org/10.1175/1520-0485(2003)033<2341:RSFTAC>2.0.CO;2.

——, and K. Speer, 2012: Closure of the meridional overturning circulation through Southern Ocean upwelling. *Nat. Geosci.*, **5**, 171–180, https://doi.org/10.1038/ngeo1391.

——, A. Adcroft, C. Hill, L. Perelman, and C. Heisey, 1997: A finite-volume, incompressible Navier Stokes model for studies of the ocean on parallel computers. *J. Geophys. Res.*, **102**, 5753–5766, https://doi.org/10.1029/96JC02775.

——, D. Jamous, and J. Nilsson, 1999: Reconciling thermodynamic and dynamic methods of computation of water-mass transformation rates. *Deep-Sea Res. I*, **46**, 545–572, https://doi.org/10.1016/S0967-0637(98)00082-X.

——, J. R. Scott, A. Romanou, M. Kelley, and A. Leboissetier, 2017: The dependence of the ocean's MOC on mesoscale eddy diffusivities: A model study. *Ocean Modell.*, **111**, 1–8, https://doi.org/10.1016/j.ocemod.2017.01.001.

Marsland, S. J., H. Haak, J. H. Jungclaus, M. Latif, and F. Röske, 2003: The Max-Planck-Institute global ocean/sea ice model with orthogonal curvilinear coordinates. *Ocean Modell.*, **5**, 91–127, https://doi.org/10.1016/S1463-5003(02)00015-X.

Marzocchi, A., and M. F. Jansen, 2017: Connecting Antarctic sea ice to deep-ocean circulation in modern and glacial climate simulations. *Geophys. Res. Lett.*, **44**, 6286–6295, https://doi.org/10.1002/2017GL073936.

Mikolajewicz, U., and Coauthors, 2012: LGM simulations with the MPI-ESM. *Third Int. Conf. on Earth System Modelling*, Hamburg, Germany, MPI, 3ICESM-192-1, http://meetingorganizer.copernicus.org/3ICESM/3ICESM-192-1.pdf.

Muglia, J., and A. Schmittner, 2015: Glacial Atlantic overturning increased by wind stress in climate models. *Geophys. Res. Lett.*, **42**, 9862–9868, https://doi.org/10.1002/2015GL064583.

Munday, D. R., H. L. Johnson, and D. P. Marshall, 2013: Eddy saturation of equilibrated circumpolar currents. *J. Phys. Oceanogr.*, **43**, 507–532, https://doi.org/10.1175/JPO-D-12-095.1.

Munk, W. H., 1966: Abyssal recipes. *Deep-Sea Res. Oceanogr. Abstr.*, **13**, 707–730, https://doi.org/10.1016/0011-7471(66)90602-4.

Nakano, H., and N. Suginohara, 2002: Effects of bottom boundary layer parameterization on reproducing deep and bottom waters in a world ocean model. *J. Phys. Oceanogr.*, **32**, 1209–1227, https://doi.org/10.1175/1520-0485(2002)032<1209:EOBBLP>2.0.CO;2.

Newsom, E. R., and A. F. Thompson, 2018: Reassessing the role of the Indo-Pacific in the ocean's global overturning circulation. *Geophys. Res. Lett.*, **45**, 12 422–12 431, https://doi.org/10.1029/2018GL080350.

Nikurashin, M., and G. Vallis, 2012: A theory of the interhemispheric meridional overturning circulation and associated stratification. *J. Phys. Oceanogr.*, **42**, 1652–1667, https://doi.org/10.1175/JPO-D-11-0189.1.

Nurser, A. G., and M.-M. Lee, 2004: Isopycnal averaging at constant height. Part I: The formulation and a case study. *J. Phys. Oceanogr.*, **34**, 2721–2739, https://doi.org/10.1175/JPO2649.1.

Oka, A., H. Hasumi, and A. Abe-Ouchi, 2012: The thermal threshold of the Atlantic meridional overturning circulation and its control by wind stress forcing during glacial

climate. *Geophys. Res. Lett.*, **39**, L09709, https://doi.org/10.1029/2012GL051421.

Otto-Bliesner, B., C. Hewitt, T. Marchitto, E. Brady, A. Abe-Ouchi, M. Crucifix, S. Murakami, and S. Weber, 2007: Last Glacial Maximum ocean thermohaline circulation: PMIP2 model intercomparisons and data constraints. *Geophys. Res. Lett.*, **34**, L12706, https://doi.org/10.1029/2007GL029475.

Snow, K., A. M. Hogg, B. M. Sloyan, and S. M. Downes, 2016: Sensitivity of Antarctic bottom water to changes in surface buoyancy fluxes. *J. Climate*, **29**, 313–330, https://doi.org/10.1175/JCLI-D-15-0467.1.

Sueyoshi, T., and Coauthors, 2013: Set-up of the PMIP3 paleoclimate experiments conducted using an Earth system model, MIROC-ESM. *Geosci. Model Dev.*, **6**, 819–836, https://doi.org/10.5194/gmd-6-819-2013.

Sun, S., and J. Liu, 2017: Sensitivity of the Antarctic Circumpolar Current transport to surface buoyancy conditions in the North Atlantic. *Ocean Modell.*, **118**, 118–129, https://doi.org/10.1016/j.ocemod.2017.09.004.

——, I. Eisenman, and A. L. Stewart, 2018: Does Southern Ocean surface forcing shape the global ocean overturning circulation? *Geophys. Res. Lett.*, **45**, 2413–2423, https://doi.org/10.1002/2017GL076437.

Thompson, A. F., A. L. Stewart, and T. Bischoff, 2016: A multibasin residual-mean model for the global overturning circulation. *J. Phys. Oceanogr.*, **46**, 2583–2604, https://doi.org/10.1175/JPO-D-15-0204.1.

Tréguier, A.-M., M. England, S. R. Rintoul, G. Madec, J. Le Sommer, and J.-M. Molines, 2007: Southern Ocean overturning across streamlines in an eddying simulation of the Antarctic Circumpolar Current. *Ocean Sci.*, **4**, 653–698, https://doi.org/10.5194/OSD-4-653-2007.

Watanabe, M., and Coauthors, 2010: Improved climate simulation by MIROC5: Mean states, variability, and climate sensitivity. *J. Climate*, **23**, 6312–6335, https://doi.org/10.1175/2010JCLI3679.1.

Watson, A. J., G. K. Vallis, and M. Nikurashin, 2015: Southern Ocean buoyancy forcing of ocean ventilation and glacial atmospheric CO_2. *Nat. Geosci.*, **8**, 861–864, https://doi.org/10.1038/ngeo2538.

Wolfe, C. L., and P. Cessi, 2011: The adiabatic pole-to-pole overturning circulation. *J. Phys. Oceanogr.*, **41**, 1795–1810, https://doi.org/10.1175/2011JPO4570.1.

——, and ——, 2014: Salt feedback in the adiabatic overturning circulation. *J. Phys. Oceanogr.*, **44**, 1175–1194, https://doi.org/10.1175/JPO-D-13-0154.1.

Yeager, S., and G. Danabasoglu, 2014: The origins of late-twentieth-century variations in the large-scale North Atlantic circulation. *J. Climate*, **27**, 3222–3247, https://doi.org/10.1175/JCLI-D-13-00125.1.

Zhang, X., G. Lohmann, G. Knorr, and X. Xu, 2013: Different ocean states and transient characteristics in Last Glacial Maximum simulations and implications for deglaciation. *Climate Past*, **9**, 2319–2333, https://doi.org/10.5194/cp-9-2319-2013.

Supplemental Material

Journal of Climate
Surface Constraints on the Depth of the Atlantic Meridional Overturning Circulation: Southern Ocean versus North Atlantic
https://doi.org/10.1175/JCLI-D-19-0546.1

JOURNAL OF CLIMATE

Supporting Information for "Surface constraints on the depth of the Atlantic Meridional Overturning Circulation: Southern Ocean vs North Atlantic"

SHANTONG SUN * AND IAN EISENMAN

Scripps Institution of Oceanography, University of California San Diego, CA, USA

LAURE ZANNA

Department of Physics, University of Oxford, Oxford, UK
and Courant Institute of Mathematical Sciences, New York University, NY, USA

ANDREW L. STEWART

Department of Atmospheric and Oceanic Sciences, University of California Los Angeles, CA, USA

Corresponding author address: Scripps Institution of Oceanography, University of California, San Diego, CA, USA
E-mail: shantong@ucsd.edu

Introduction

This supporting information contains three figures which are discussed in the main text.

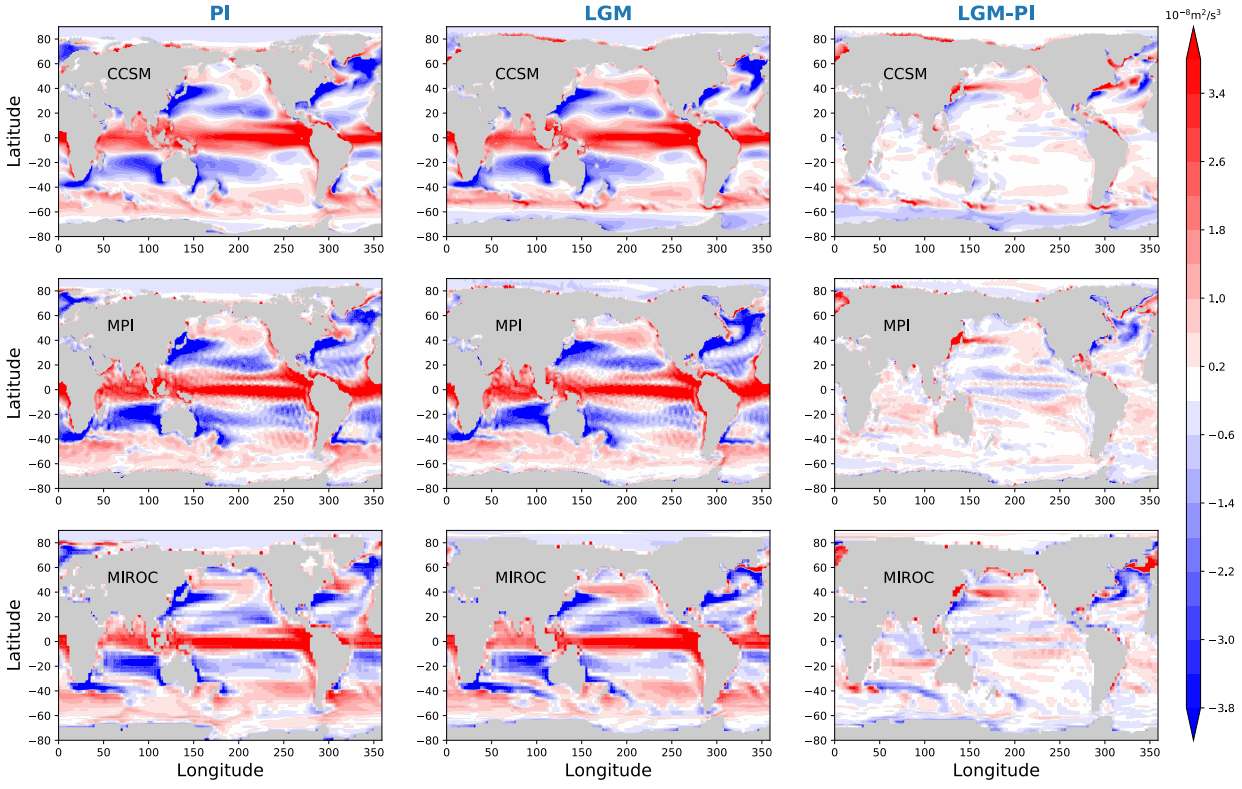

FIG. S1. Surface buoyancy flux in the PMIP3 simulations for the PI climate (left), the LGM climate (center), and their difference (right). Three models are included: CCSM4 (top), MPI-ESM (middle), and MIROC-ESM (bottom).

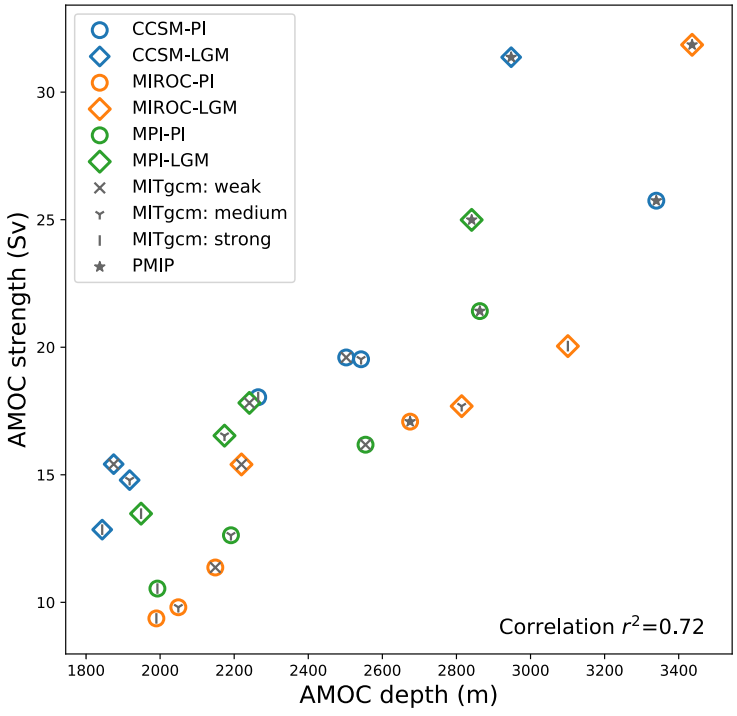

FIG. S2. Comparison of the AMOC depth with the AMOC strength, which is defined as the maximum of the AMOC streamfunction below 500 m. The PMIP3 simulations and the MITgcm simulations discussed in Section 3 are plotted.

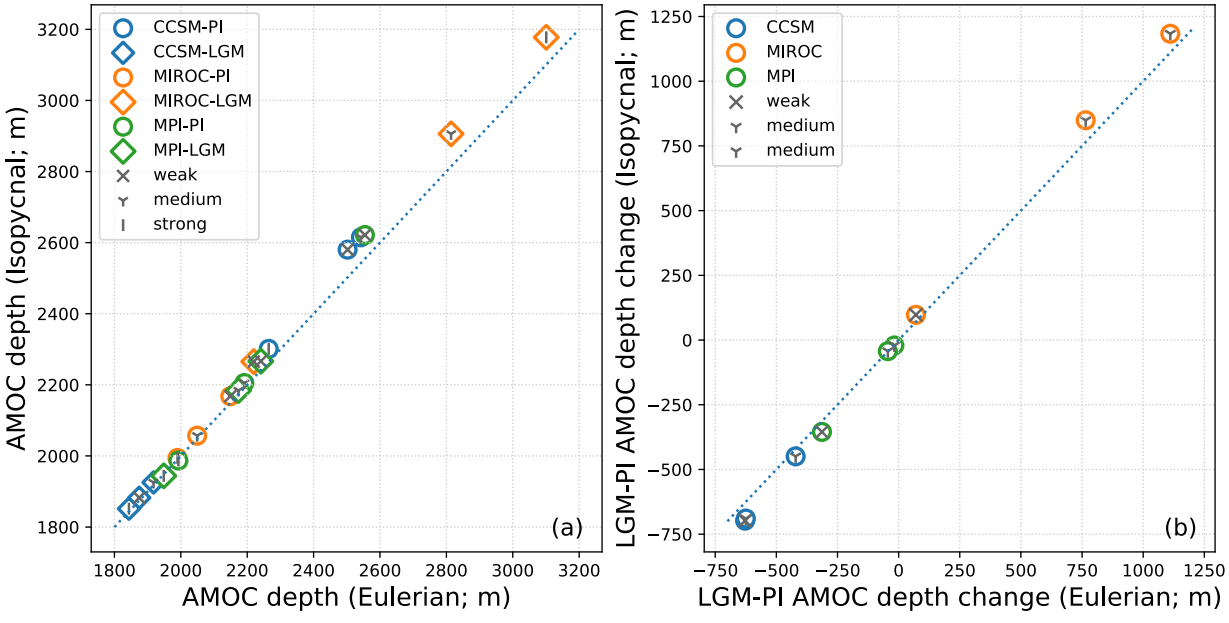

FIG. S3. Comparison of (a) the AMOC depth and (b) the LGM–PI AMOC depth change, plotted as the value calculated using the isopycnal overturning circulation versus the value calculated using the Eulerian-mean overturning circulation.